Dynamic effect in the fatigue fracture of viscoelastic solids

Oiang Guo¹, Julien Caillard², Davide Colombo², Rong Long^{1*}

¹Department of Mechanical Engineering, University of Colorado Boulder, Colorado, 80309, USA.

²Manufacture Française des Pneumatiques Michelin, Centre de Technologies Europe, Clermont

Ferrand Cedex 9, 63040, France

*Corresponding author: rong.long@colorado.edu

Abstract:

Crack growth in viscoelastic solids under cyclic loading tends to be faster than that under static

loading with the same amplitude. This phenomenon, known as "dynamic effect", is a key

mechanism underlying the fatigue fracture of soft viscoelastic polymers, but its physical nature

remains a mystery. We develop a scaling theory to delineate how viscoelastic dissipation associated

with crack growth is governed by the coupling between three time-dependent processes: cyclic

loading, crack growth and viscoelastic creep. In the limit of slow crack growth and slow cyclic

loading, a simple integral equation is derived to predict the crack growth velocity under different

cyclic loading frequencies.

Keywords: fatigue; viscoelasticity; fracture criterion; dissipation; crack growth velocity; spatial

hysteresis.

1

1. Introduction

Crack growth in viscoelastic solids is a fundamental problem for the failure analysis of rubber and other soft polymers. Fatigue fracture, referring to crack growth under prolonged cyclic loading, is a failure mode of particular relevance to applications such as tires, sealants, and biomedical implants. Despite the extensive experimental studies on fatigue fracture in rubber [1–5], predictive theories are still lacking. Most existing analyses of viscoelastic fracture focus on steady-state crack growth under static loading [6–10]. The underlying physics is manifested in the coupling between two time scales: one associated with the crack growth velocity V and the other being the viscoelastic relaxation time τ . This coupling can be visualized using the "viscoelastic trumpet" proposed by de Gennes [8]. Briefly, for a steadily growing crack, the crack tip is surrounded by a region with highly amplified strain rate within which the material behaves as a "hard solid". Far away from the crack tip, the material is relaxed and hence behaves as a "soft solid". Bridging the "hard solid" and "soft solid" regions is a "liquid region" where viscoelasticity dissipates energy. Such dissipation implies that additional energy is required to drive crack growth, as stated by the equation $G = G_0 + G_D(V)$, where G is the total energy release rate, i.e., energy available for driving a unit area of crack growth, G_0 is the energy release rate delivered to the crack tip, and G_D is due to viscoelastic dissipation and hence sensitive to the crack velocity V. To maintain quasi-static crack growth, G_0 should be equal to the intrinsic fracture energy of the solid Γ_0 (energy per unit area), which is regarded as a material constant. Further analyses on G_D have shown that in an infinite domain $G/G_0 = \phi(V\tau/l)$ where l is the length scale associated with the fracture processes at the crack tip and the function ϕ can be solved by integrating dissipation over the viscoelastic domain [8,10].

In case of fatigue fracture, G is a periodic function of time t. It is tempting to use the relation $G/G_0 = \phi(V\tau/l)$ for static crack growth to predict the length of crack extension per cycle, i.e., dc/dN where c is the crack length and N is the cycle number. However, caution must be taken as shown in a seminal work by Lake and Lindley [11]. They performed both cyclic and static crack growth experiments for a synthetic rubber (i.e., styrene-butadiene) that is unfilled and non-crystallizing and hence can be considered as a viscoelastic solid. From these experiments, they measured the function of dc/dN versus G for cyclic crack growth, and V_s (or dc/dt) versus G for static crack growth. They used the function $V_s(G)$ for static crack growth to predict the cycle crack growth rate, denoted as $(dc/dN)_s$, by calculating $dc/dt = V_s$ at any time during a cycle and integrating dc/dt over

one cycle. Interestingly, $(dc/dN)_s$ was found to be much smaller than the actual dc/dN. To account for the discrepancy, Lake and Lindley concluded an extra term $(dc/dN)_d$ must exist and named it as the "dynamic component" of crack growth, i.e.,

$$dc/dN = (dc/dN)_s + (dc/dN)_d.$$
(1)

Experimental data revealed that $(dc/dN)_d$ is negligible at low frequency, but becomes dominant at high frequency, e.g., $(dc/dN)_s$ is less than 3% of the total dc/dN at high frequency [11]. Here "dynamic" implies cyclic loading rather than inertial effects. It has also been observed that $(dc/dN)_d$ is sensitive to the waveform of the cyclic loading [12]. Despite the clear experimental evidence, the physical nature of the dynamic effect causing $(dc/dN)_d$ remains a long standing mystery.

The goal of this work is to develop a scaling theory to explain the underlying physics of the dynamic component $(dc/dN)_d$. Given that the synthetic rubber used in Lake and Lindley [11] was unfilled and non-crystallizing, we attribute $(dc/dN)_d$ to viscoelasticity. From a scaling analysis perspective, cyclic loading introduces an additional time scale (e.g., the cycle period T) to the coupling between crack velocity V and relaxation time τ . Interplay between the three time scales holds the key towards understanding the viscoelastic dissipation associated with cyclic crack growth. In the following, we first present a fracture criterion derived from energy balance and then introduce two concepts, "spatial hystersis" and "phantom state", to enable the definitions of G and G_D for cyclic crack growth (Section 2). In Section 3, we use a Finite Element (FE) model to verify the energy balance theory and to demonstrate the dynamic effect of cyclic loading. Based on the energy balance theory, we derive an integral equation governing the crack velocity during a loading cycle. In the limit of slow crack growth and slow cyclic loading, this integral equation can be greatly simplified and numerically solved to obtain the crack growth velocity under different cyclic loading frequencies. It should be emphasized that we do not seek quantitative prediction of the experimental data in Lake and Lindley [11], which would require a detailed calibration of the viscoelastic behavior since synthetic rubber typically exhibit a wide spectrum of relaxation times. Instead, our focus is on using the scaling theory to capture the qualitative trend of dynamic effect found in FE simulations based on a simple viscoelastic model. This can pave the way for future development of more sophisticated theories to achieve quantitative prediction. In Section 4, we conclude by summarizing the theory and outlining limitations and potential improvements.

2. Energy Balance Theory

Existing theories of viscoelastic fracture [6–10] focus on steady-state crack growth under static loading in which material far away from the crack tip, referred to as the "far field", is relaxed and viscoelastic dissipation occurs only around the moving crack tip. However, under cyclic loading, viscoelastic dissipation can occur in the far field even in the absence of crack growth. A theoretical challenge is on how to separate the dissipation due to cyclic loading and that due to crack growth, which is addressed here. Without loss of generality, we consider the ideal "pure shear" geometry (see Fig. 1a) consisting of an infinitely wide thin sheet with a semi-infinite crack. A vertical displacement Δ , or equivalently, a nominal stretch ratio $\lambda \equiv 1 + \Delta/H$, is applied to open the crack symmetrically and drive crack growth. This configuration, known as plane stress Mode-I fracture, has been widely used in the fracture tests of rubber and soft elastomers [11,13,14]. In experiments, crack growth settles to a constant rate after a number of initial cycles. This phenomenon motivates us to assume the *quasi-steady-state* condition, where the crack extension within each loading cycle is the same and the stress and strain tensors at a material point only depend on its relative position to the crack tip and the time within a loading cycle. As detailed in Section S1 of the Supplementary Information (SI), we use the *quasi-steady-state* condition to derive the following energetic fracture criterion [15], which is valid for both elastic and inelastic materials,

$$\begin{cases} V = 0 & \text{if } G_0 < \Gamma_0 \\ V \ge 0 & \text{if } G_0 = \Gamma_0 \end{cases} \quad \text{with } G_0 \equiv \int_{-H/2}^{H/2} \int_{-\infty}^{+\infty} \left(\mathbf{\sigma} : \frac{\partial \mathbf{\epsilon}}{\partial X} \right) dX dY$$
 (2)

where σ and ε are the stress and strain tensors, respetively, and X-Y is a moving coordinate system centered at the crack tip and translates with crack.

Equation (2) presents both stress and strain in terms of tensorial quantities. For simplicity, we follow de Gennes [8] and use the normal stress and strain along the *Y*-direction, i.e., σ and ε , as scaling representations of the multi-axial stress and strain fields. Therefore, Eq. (2) is simplified to $G_0 = \int_{-H/2}^{H/2} \xi(Y) \, dY$ where $\xi(Y) = \int_{-\infty}^{+\infty} \sigma(\partial \varepsilon/\partial X) \, dX$. To understand what contributes to G_0 , we schematically plot σ versus ε along a horizontal line with a constant *Y* where $\varepsilon = 0$ at $X = -\infty$ and $\varepsilon = \lambda - 1$ at $X = +\infty$ (see Fig.1a). A peak stress (or strain) is expected due to stress concentration at the crack tip. The closer to the crack tip (i.e., smaller |Y|), the higher the peak stress is. For elastic

materials, there is a one-to-one relationship between σ and ε . Consequently, the integral, $\xi(Y)$ is independent of the peak stress and thus is uniform with Y. Specifically, for linear elastic materials $\xi = \sigma_\infty \varepsilon_\infty / 2$, where $\sigma_\infty = \sigma(X = +\infty)$ and $\varepsilon_\infty = \varepsilon(X = +\infty)$. In this case, Eq. (2) degenerates to $G_0 = \sigma_\infty \varepsilon_\infty H / 2$ which recovers the well-known energy release rate equation for pure shear geometry [13,14,16]. Note that the result that $G_0 = \sigma_\infty \varepsilon_\infty H / 2$ for linear elastic materials can also be derived by applying the J-integral to the pure shear geometry, as illustrated in Rice [17]. For inelastic materials, however, a stress may correspond to two different strains depending on the deformation history, leading to hysteretic stress-strain curves along a horizontal line. Such hysteresis does not refer to the temporal history at a fixed material point. Rather, it is regarding the spatial distribution from $X = -\infty$ to $X = +\infty$ and thus is termed as the "spatial hysteresis". When spatial hysteresis is present, ξ depends not only on σ_∞ and ε_∞ , but also on the peak stress that varies with Y.

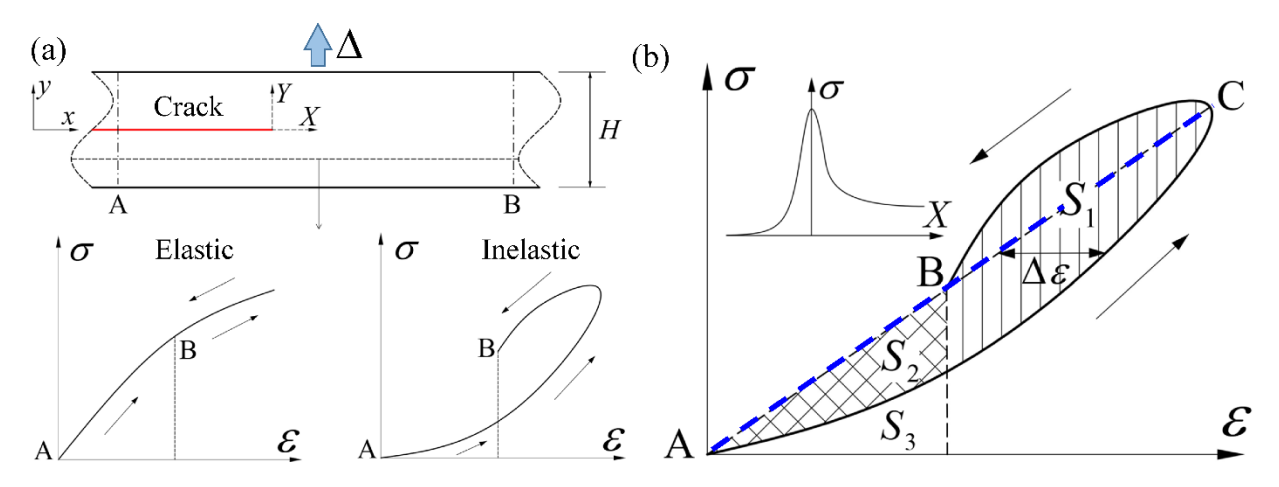


Figure 1 Spatial hysteresis. (a) Ideal pure shear fracture geometry and schematics showing the stress and strain along a horizontal line. (b) Spatial hysteresis along a horizontal line. The blue dashed line connecting A and C represents the phantom state, while the solid line represents the actual state.

The spatial hysteresis is completely attributed to crack growth. To demonstrate this point, we assume linear viscoelasticity and introduce a fictious state where the same crack is subjected to the same external loading but its growth is suppressed. This fictious state will be referred to as the "phantom state" hereafter. In this state, the fields are determined by the external loading and the presence of the crack, but not by crack growth. Spatial hysteresis is absent in the phantom state, because each material point in the phantom state follows the same oscillatory strain history but

different amplitudes. Therefore, at a given time, the stress and the strain at all material points are related by the same dynamic modulus. Therefore, in the phantom state, the integral in Eq. (2) reduces to $G_0 = \sigma_\infty \varepsilon_\infty H/2$. This is like the case of linear elastic materials but with a subtle difference: σ_∞ and ε_∞ are related by the dynamic modulus which is sensitive to the loading frequency. In other words, even under the assumption of quasi-steady-state condition, the far field is not necessarily in the relaxed state, which is different from the steady-state condition under static loading. Nevertheless, we can always define a phantom state (without crack growth) corresponding to the actual state (with crack growth) at any moment during a loading cycle. These two states share the same stress and strain fields far away from the crack tip, but exhibit different fields near the crack tip due to the different status of crack growth. To distinguish them, we denote the stress and strain fields in the phantom state as $\bar{\sigma}$ and $\bar{\varepsilon}$. Based on the discussions above, we apply Eq. (2) to the phantom and actual states and write the difference as:

$$\frac{\sigma_{\infty}\varepsilon_{\infty}H}{2} - G_0 = \int_{-H/2}^{H/2} \int_{-\infty}^{+\infty} \left(\overline{\sigma} \frac{\partial \overline{\varepsilon}}{\partial X} - \sigma \frac{\partial \varepsilon}{\partial X}\right) dXdY.$$
 (3)

Eq. (3) reflects two important implications of introducing the phantom state. First, for viscoelastic solids under cyclic loading, dissipation can occur even in the far field. As a result, the total energy release rate G is not well defined, since it is difficult to delineate the energy consumed by crack propagation and that dissipated by cyclic loading. By introducing the phantom state, we can unambiguously identify G as the energy release rate that can be delivered to the crack tip in the phantom state, which is equal to $\sigma_{\infty} \varepsilon_{\infty} H/2$ (see Eq. (3)). Second, Eq. (2) requires the full stress and strain fields over the entire geometry, which can be difficult to obtain for viscoelastic solids under cyclic loading. By introducing the phantom state, we obtain Eq. (3) in which the integrand, $\bar{\sigma}(\partial \bar{\varepsilon}/\partial X) - \sigma(\partial \varepsilon/\partial X)$, is only non-zero near the crack tip, since the phantom and actual states should cancel each other in the far field. This feature allows us to avoid determining the full stress and strain fields over the entire geometry and focus on the crack tip region. Applying the correspondence principle extended by Graham [18] for problems with moving boundaries to a growing crack and assuming no crack surface contact during unloading [19], we conclude that the stress field near the crack tip in the actual and phantom states still follows the K-field in linear elastic fracture mechanics. Therefore, we hypothesize that $\sigma(X,Y,t) = \bar{\sigma}(X,Y,t) = K(t)f(X,Y)$ near the crack tip, where K is the stress intensity factor and f(X,Y) represents the spatial distribution of the *K*-field. More discussions on justifying and verifying this assumption are provided in Section S3 of the SI. Consequently, we obtain the following energy balance equation:

$$G - G_0 = G_D = -\int_{-H/2}^{H/2} \int_{-\infty}^{+\infty} \left(\sigma \frac{\partial \Delta \varepsilon}{\partial X} \right) dX dY, \qquad (4)$$

where $\Delta \varepsilon = \varepsilon - \bar{\varepsilon}$ is the strain differential between the actual and phantom states. By introducing the phantom state, we have unambiguously defined G and G_D for cyclic loading.

Although the actual and phantom states share the same crack tip stress field at a given time t, material points in these two states have experienced different stress histories (see Section S3 of the SI). For example, consider a material point located at (X, Y) at the current time t. The stress experienced by this point at any prior time $t'(\le t)$ is $\sigma = K(t')f(X + \Delta c(t, t'), Y)$ in the actual state and $\bar{\sigma} = K(t')f(X, Y)$ in the phantom state, where $\Delta c(t, t') \equiv c(t) - c(t')$ is the length of crack extension from t' to t. Such a difference in stress history leads to the differential strain $\Delta \varepsilon$, which is the key mechanism underlying the spatial hysteresis. As schematically illustrated in Fig.1b, along a horizontal line AB on the sample, the phantom state yields a linear relation between $\bar{\sigma}$ and $\bar{\varepsilon}$ with the slope given by the dynamic modulus. In the actual state, crack growth results in negative $\Delta \varepsilon$ ahead C (i.e., location of the peak stress) and positive $\Delta \varepsilon$ behind C, thus expanding the stress strain curve into a spatial hysteresis loop. Using the areas S_1 , S_2 and S_3 marked on Fig.1b, G, G_0 and G_D are equal to the integral of $S_2 + S_3$, $S_3 - S_1$, and $S_1 + S_2$ along the Y axis, respectively. Physically the effects of cyclic loading and crack growth are manifested in the time functions of K(t) and c(t), respectively. Their coupling is encoded in the strain differential $\Delta \varepsilon$ between the actual and phantom states.

To put our theory into perspective, we note that existing theories for steady-state crack growth under static loading can be categorized into two approaches: i) cohesive zone and ii) energy balance. The cohesive zone approach [19,20] focuses on analyzing the opening displacement of a cohesive zone at the crack tip. The energy balance approach [8–10] considers a featureless crack and integrates the energy dissipation due to crack growth by assuming the stress near the crack tip follows K-field. We adopt the energy balance approach to highlight the physics of how cyclic loading affects energy dissipation around the crack tip. By introducing two concepts: spatial hysteresis and phantom state, we have extended the energy balance approach from static loading to cyclic loading.

Although it appears that the energy balance approach does not require an intrinsic length scale at the crack tip, this is not the case. As summarized in a historical perspective by Hui et al. [21], a cut-off length *l* must be introduced to exclude a small region around the crack tip from the integral for energy dissipation, otherwise the crack tip singularity would lead to a paradox noted by Rice [22]. Conceptually, the cut-off length *l* is similar to the cohesive zone size in that both the energy balance and cohesive zone approaches need to introduce an intrinsic length scale to regularize the crack tip singularity. Recent studies [21,23,24] comparing the energy balance and cohesive zone approaches showed that these two approaches give similar results (except at low crack velocity) provided that the cut-off length or cohesive zone size is viewed as a fitting parameter rather than a prescribed constant. Within the energy balance approach, there are different ways to impose the cut-off length *l*. For example, de Gennes [8] assumed a constant cut-off length and attribute it to the fracture process zone at the crack tip, while Persson and Brener [9] assumed a maximum stress at the crack tip which resulted in an increasing cut-off length *l* with the energy release rate *G*. As will be discussed in the next section, we also need to introduce a cut-off length when carrying out the integral in Eq. (4). For simplicity, we follow de Gennes [8] and assume a constant cut-off length.

A common problem for the energy balance and cohesive zone approaches is that the cut-off length (or the cohesive zone size in the limit of low crack velocity) needs to be unrealistically small (on the order angstroms) for the viscoelastic fracture theories to fit experimental data [21]. In a review paper [6], Knauss pointed out limitations of applying linear viscoelasticity at the crack tip and that nonlinear viscoelasticity may be the key to address this problem, but this remains an open problem. Since our goal is to develop a scaling theory, we still adopt linear viscoelasticity but keep in mind that the cut-off length *l* may be unrealistically small.

3. Dynamic Effect of Cyclic Loading

Equipped with the energy balance theory, we are now ready to study the dynamic viscoelastic effect in cyclic crack growth. To demonstrate that the dynamic effect observed by Lake and Lindley[11] can be qualitatively modeled using a simple viscoelastic model, we first perform FE simulations using ABAQUS (Simulia, Providence, RI, USA). The FE model (see Fig.2a) consists of a wide thin sheet (width: L; height: H) clamped by rigid plates at the top and bottom edges. A pre-crack with length c is introduced in the middle of the sheet's left edge. To simulate crack

growth, we introduce a cohesive zone directly ahead of the crack tip by introducing a layer of cohesive elements. The cohesive elements follow a bilinear traction-separation law featuring a peak cohesive traction $\sigma_{\rm cm}$ and a maximum separation $\delta_{\rm m}$. Consequently, the intrinsic fracture energy Γ_0 is given by $\Gamma_0 = \sigma_{\rm cm} \delta_{\rm m}/2$. Viscoelasticity is introduced by assuming a simple model whose rheological schematic is shown in Fig.2b. This model, featuring a single relaxation time τ , an instantaneous modulus E_0 and a long-term relaxed modulus E_{∞} , was implemented using Simo's approach of quasi-linear viscoelasticity [25]. More details on the FE model gometry, cohesive and material parameters, simulation procedures and data processing are provided in Section S2 of the SI. We consider both static and cyclic loadings by prescribing the nominal stretch ratio $\lambda \equiv 1 + \Delta/H$ (Fig.2c). The applied energy release rate is calculated using $G = \sigma_{\infty} \varepsilon_{\infty} H/2$ where $\varepsilon_{\infty} = \lambda - 1$. Under static loading, the crack growth settles to a steady state with constant velocity V_s (Fig.S2) after an initial transient stage. By varying λ , an empirical relation between G and V_s , $V_s(G)$, can be established (see inset of Fig.2d). Note that we normalize V_s by δ_m/τ where δ_m is the maximum separation of the cohesive element. In the literature [21], V_s is often normalized by the cohesive zone size and relaxation time so that it reflects the characteristic strain rate near the crack tip. Since our purpose here is to present the simulation results in a dimensionless form rather than to reveal physical significance, we choose to use the prescribed constant δ_m for normalizing V_s . Under cyclic loading, we apply triangular periodic functions for $\lambda(t)$ that is bounded by $\lambda_{min} = 1$ and λ_{max} and has a period of T. After a few cycles, the cyclic crack growth is observed to settle at a constant rate dc/dN (Fig.S3).

To quantify the dynamic viscoelastic effect, we first determine $(dc/dN)_s$ using the empirical relation $V_s(G)$ with the periodic function G(t) (see Section S2 of the SI) and calculate the ratio $\beta = (dc/dN)/(dc/dN)_s$. Our simulation results in Fig.2d show that β approaches one when the period T is much larger than the relaxation time τ but can be substantially larger than one when T becomes comparable to τ , which is consistent with the trend of experimental observations in Lake and Lindley [11]. To verify our fracture criterion, we compute G_0 during a loading cycle using Eq. (2) and the stress and strain fields obtained from the FE results, and compute G and G_D by $G = \sigma_\infty \varepsilon_\infty H/2$, and $G_D = G - G_0$, respectively. The results are shown in Fig.2e. We observe that during crack growth G_0 is bounded by Γ_0 , while G can exceed Γ_0 . The duration when $G_0 = \Gamma_0$ overlaps that of crack growth. The excessive energy release rate $G - G_0$ is consumed by the viscoelastic

dissipation G_D . For comparison, we repeat the simulation but increase the inrinsic fracture energy to a sufficiently large value Γ_0^* (= $3\Gamma_0$) so that crack growth is suppressed, which effectively recovers the phantom state. In this case (Fig.2f), G is approximately equal to G_0 while G_D is negligible.

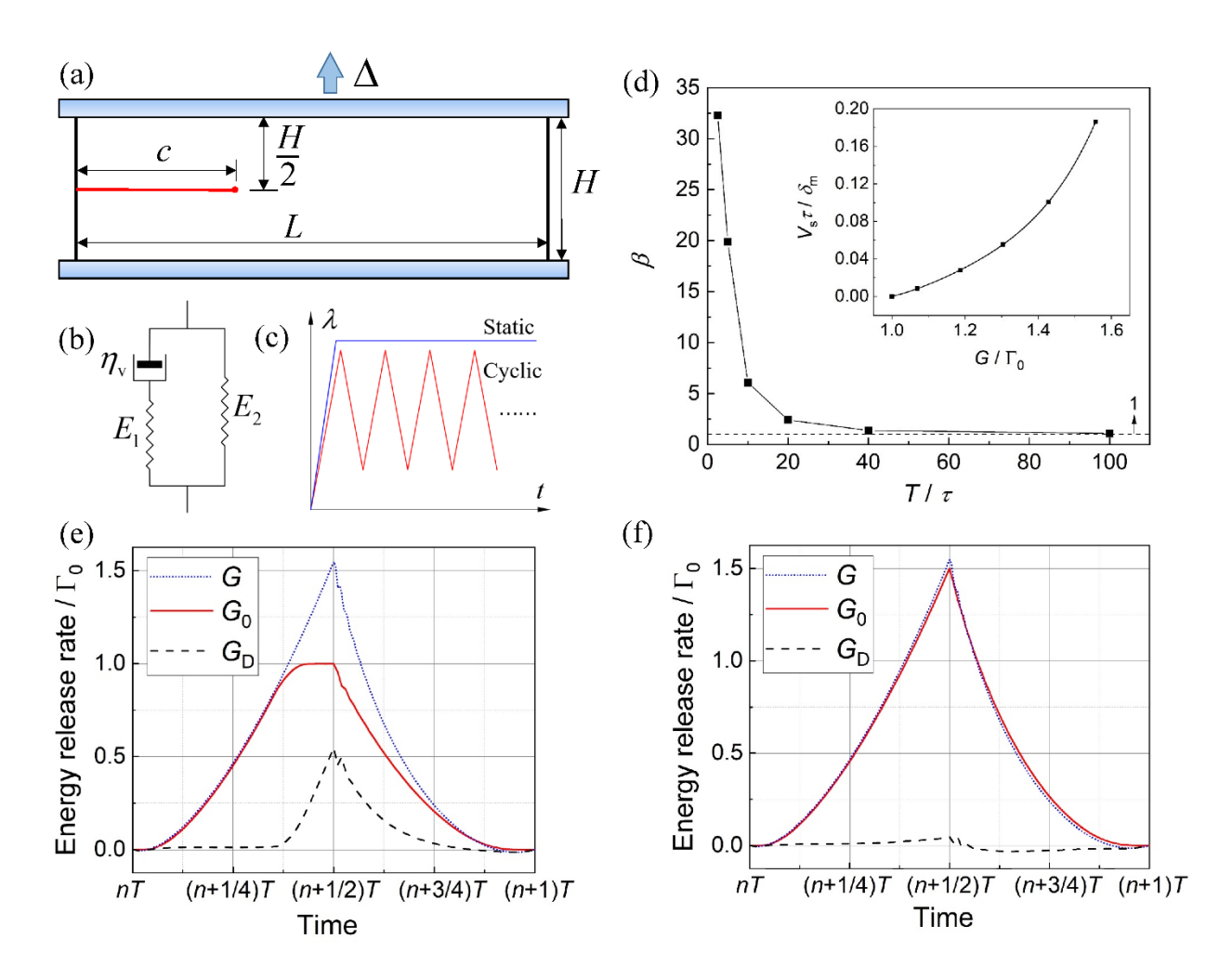


Figure 2 FE simulation and results. (a) Model geometry and dimensions. (b) Schematic of the viscoelastic model. (c) Static and cyclic loading processes. (d) FE results of the ratio β defined as $(dc/dN)/(dc/dN)_s$. The inset shows the empirical ration between V_s and G for static loading. Note that V_s is normalized by δ_m/τ where δ_m is the maximum separation of the cohesive element. (e-f) G, G_0 and G_D computed using the FE results during a loading cycle for the (e) actual state and (f) phantom state. To suppress crack growth in the phantom state, we increase the instrinsic fracture energy to $\Gamma_0^* = 3\Gamma_0$. However, to facilitate comparison, we normalize the energy release rates in both (e) and (f) by Γ_0 .

Our energy balance theory allows us to qualitatively capture the dynamic viscoelastic effect. By using the stress history for the actual and phantom states to calculate the strain differential $\Delta\varepsilon$ and then substituting it into Eq. (4), we obtain the following integral equation for the crack length c(t) (see Section S4 of the SI):

$$G - G_0 = -K(t) \int_{-H/2}^{H/2} \int_{-\infty}^{+\infty} \dot{J}(t - t') K(t') f(X, Y) \left[\frac{\partial f}{\partial X} (X + \Delta c(t, t'), Y) - \frac{\partial f}{\partial X} (X, Y) \right] dt' dX dY, \quad (5)$$

where J(t) is the creep compliance function and $\dot{J} = dJ/dt$. Recall that f(X,Y) represents the spatial distribution of the K-field (see Eq. (S14) in the SI). Eq. (5) is valid for general cyclic loadings, but numerical solution of this equation can be challenging. To obtain physical insights, we focus on the limit of slow crack growth and slow loading. After a lengthy derivation detailed in Section S4 of the SI, we obtain the following simplified equation:

$$G(t) - G_0 = K(t)C_f \int_{-\infty}^{t} \tilde{J}(t - t')K(t')V(t')dt', \qquad (6)$$

where C_f is the spatial integral of the K-field distribution f(X,Y), $\tilde{J}(t) = J(t) - J(t \to +\infty)$ is the non-equilibrium portion of the creep function J(t), and V(t) is the crack propagation velocity at time t. As detailed in Section S4 of the SI, C_f is obtained by integrating a field involving f(X,Y) and its spatial gradients. When carrying out the integration, we introduce a constant cut-off length l representing the length of the fracture process zone [8,10], as discussed in Section 2. We find that C_f is a negative constant that scales as $C_f \sim -1/l$. The slow crack propagation and slow loading conditions required by Eq. (6) implies $V/l \ll 1/\tau_c$ and $\dot{K}/K \ll 1/\tau_c$, respectively, where τ_c is the characteristic time for the creep function, also known as the creep retardation time. For the standard linear solid model in Fig. 2c, τ_c is related to the relaxation time τ by $\tau_c = \eta \tau$ where $\eta \equiv E_0/E_\infty$. Equation (6) highlights the coupling between the three time scales associated with cyclic loading, viscoelastic creep and crack propagation. It is worth mentioning that Knauss [6] showed the dynamic viscoelastic effect would be absent (i.e., $\beta = 1$) if $\dot{K}/K \ll V/2l$. Even though Eq. (6) requires that both V/l and \dot{K}/K are much smaller than $1/\tau_c$, it is still possible for Eq. (6) to capture dynamic viscoelastic effect by allowing $\dot{K}/K \sim V/l$.

We numerically solve Eq. (6) by prescribing G(t) and K(t) according to the external loading. Generally speaking, under cyclic loading the material far away from the crack tip (i.e., the far field) is not in the relaxed, but is governed by the dynamic modulus set by the loading frequency. In this case, the relation between G(t) and K(t) may not be straightforward. However, because of the *slow loading* condition $(\dot{K}/K << 1/\tau_c)$ assumed for Eq. (6), the loading cycle is much longer than the relaxation time. Therefore, it is reasonable to assume the far field is in the fully relaxed state under *slow loading*, yielding that $G(t) = (K(t))^2/E_{\infty}$. Furthermore, we apply the standard linear solid model with $\tilde{J}(t) = -(\eta - 1)e^{-t/\tau_c}/E_0$. Details of the numberical solution procedures are given in Section S5 of the SI. It is informative to first consider the static loading case where G, K and V are constants, for which Eq. (6) results in $G - G_0 = K^2 |C_f|V\tau_c(\eta - 1)/E_0$. Using $\tau_c = \eta \tau$, $|C_f| \sim 1/l$ and assuming $\eta >> 1$ [8], we obtain $G - G_0 \sim (K^2/E_0)V\tau\eta^2/l$, which recovers the scaling relation in Saulnier et al. [10] in the limit of slow crack propagation (i.e., $V << l/\tau_c = l/\eta \tau$).

Under cyclic loading, we assign periodic functions for G(t) and K(t) to numerically solve for the crack velocity V using Eq. (6). To demonstrate that Eq. (6) can capture the trend of FE results in Fig. 2d, we implement the same G(t) and viscoelastic parameters as those in the FE model and set G_0 to be the same as the Γ_0 in the FE model which is specified by the cohesive zone. It should be emphasized that our theory does not use cohesive zone to model the crack tip fracture process, but simply enforces a constant cut-off length l at the crack tip. On the other hand, the cohesive zone size in the FE model may vary with crack velocity. For example, it has been shown that the cohesive zone size can increase with crack velocity by a ratio up to $\eta = E_0/E_\infty$ [6,21]. This is inconsistent with the constant cut-off length l assumed in the theory. To address this issue, we have adopted a small value for η (i.e., $\eta = 2$, see Section S2 and S5 of the SI) in both the FE model and the numerical solutions for Eq. (6), which can limit the variation of cohesive zone size in the FE model while still capturing viscoelasticity. As a reference, more realistic values of η for elastomers should fall in the range of 10 to 10³. Solutions of crack velocity in a loading cycle obtained from Eq. (6) are shown in Fig.3a. The static limit, obtained using $(G(t) - G_0)/G(t) = |C_f|\tau(\eta - G_0)/G(t)$ 1)V(t) is also plotted for comparison. When T/τ increases, the crack velocity V approaches the static limit. In constrast, when T is comparable to τ , the crack velocity V is highly skewed towards the loading part of the cycle and quickly decays to 0 once the unloading starts, which is consistent with the FE results. By integrating the crack velocity over one period T, we calculated the crack growth per cycle dc/dN, as well as the static counterpart $(dc/dN)_s$, and then obtained the dynamic amplification factor $\beta = (dc/dN)/(dc/dN)_s$, as shown in Fig.3b. The data qualitatively capture the trend that β approaches one when $T/\tau >> 1$, but rapidly increases as T/τ decreases. Recall that Eq. (6) requires the conditions of slow crack growth ($V/l << 1/\tau_c$) and slow loading ($\dot{K}/K << 1/\tau_c$). Therefore, the theoretical solution is not expected to be valid as T/τ approaches 1 since it would violate the slow loading condition. However, the FE results are not subjected to this restriction and should be valid for the full range of T/τ . This explains the increasing discrepancy between FE result and theoretical solution as T/τ is reduced.

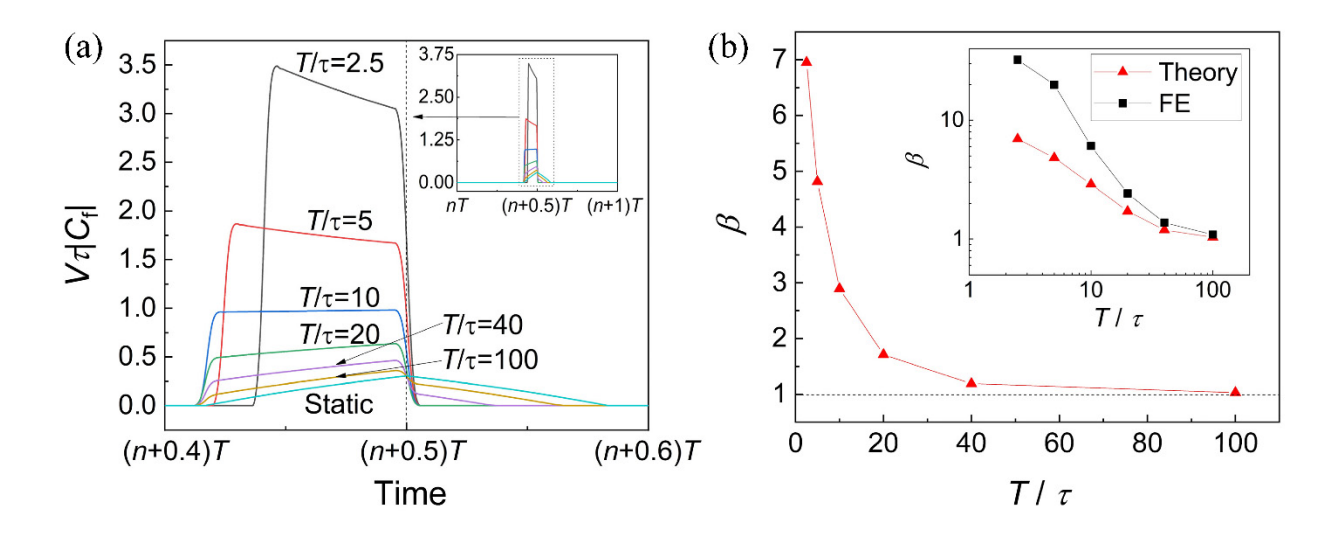


Figure 3 Numerical solutions of crack velocity. (a) The evolution of V during a loading cycle. Note that V is normalized by $1/\tau |C_f|$. The inset shows a zoomed-out view of the entire loading cycle. (b) The dynamic viscoelastic amplification factor β defined as $(dc/dN)/(dc/dN)_s$. The inset shows the comparation with FE simulaton results.

4. Discussions and Conclusion

In summary, we formulate a scaling theory to qualitatively capture the dynamic viscoelastic effect in cyclic crack growth. By introducing the concepts of spatial hysteresis and phantom state, the theory separates the viscoelastic dissipation induced by cyclic loading and crack growth, which enables us to unambiguously define G, G_0 and G_D for cyclic crack growth. Our analysis leads to an integral equation governing the crack growth velocity, which can be numerically solved to predict the cylic crack growth rate during fatigue fracture.

Since the scaling theory is based on several simplifying assumptions, limitations due to these assumptions should be addressed to achieve quantitative agreement with experimental data. These

potential extensions are outlined in the following. First, the multi-axial state of crack tip stress and strain is not considered in the current theory, but can be taken into account by keeping the stress and strain in the tensorial form. Second, we have assumed a constant cut-off length *l* that is independent of crack velocity. Dependence of the cut-off length *l* on crack velocity can be incorporated by following Persson and Brener [9] and imposing a maximum stress at the crack tip rather than a fixed cut-off length. Third, we have assumed that no crack surface contact occurs during unloading. If crack surface contact occurs, validity of the extended correspondence principle needs to be reexamined. Specifically, the case of crack surface contact was considered by Schapery [26] where an alternative form of the correspondence principle was given and later used to study crack closing [27,28]. How to extend our theory requiring only the crack tip K-field to cases with crack surface contact needs to be further studied. Fourth, numerical solution of Eq. (5) should be explored to extend the theoretical solution beyond the *slow crack groth* and *slow loading* condition. Finally, more realistic viscoelastic models should be implemented in the theory and FE model to facilitate a parametric study on the effects of viscoelastic properties, cut-off length (or cohesive zone in the FE model) and loading cycles.

Acknowledgement

This work is supported by a research grant from Michelin. R.L. is also supported by the U.S. National Science Foundation through a CAREER award (CMMI-1752449).

References

- [1] W. V. Mars, A. Fatemi, Factors that affect the fatigue life of rubber: A literature survey, Rubber Chem. Technol. 77 (2004) 391–412. https://doi.org/10.5254/1.3547831.
- [2] A.G. Thomas, Rupture of rubber. V. Cut growth in natural rubber vulcanizates, J. Polym. Sci. 31 (1958) 467–480. https://doi.org/10.1002/pol.1958.1203112324.
- [3] A.N. Gent, P.B. Lindley, A.G. Thomas, Cut growth and fatigue of rubbers. I. The relationship between cut growth and fatigue, J. Appl. Polym. Sci. 8 (1964) 455–466. https://doi.org/10.1002/app.1964.070080129.

- [4] S. Mzabi, D. Berghezan, S. Roux, F. Hild, C. Creton, A critical local energy release rate criterion for fatigue fracture of elastomers, J. Polym. Sci. Part B Polym. Phys. 49 (2011) 1518–1524. https://doi.org/10.1002/polb.22338.
- [5] L. Chazeau, J.M. Chenal, C. Gauthier, J. Kallungal, J. Caillard, About the Influence of Materials Parameters on the Ultimate and Fatigue Properties of Elastomers, in: G. Heinrich, R. Kipscholl, R. Stoček (Eds.), Adv. Polym. Sci., Springer, 2021: pp. 297–329. https://doi.org/10.1007/12 2020 80.
- [6] W.G. Knauss, A review of fracture in viscoelastic materials, Int. J. Fract. 196 (2015) 99–146. https://doi.org/10.1007/s10704-015-0058-6.
- [7] R.A. Schapery, A theory of crack initiation and growth in viscoelastic media II. Approximate methods of analysis, Int. J. Fract. 11 (1975) 369–388. https://doi.org/10.1007/BF00033526.
- [8] P.G. de Gennes, Soft Adhesives †, Langmuir. 12 (1996) 4497–4500. https://doi.org/10.1021/la950886y.
- [9] B.N.J. Persson, E.A. Brener, Crack propagation in viscoelastic solids, Phys. Rev. E Stat. Nonlinear, Soft Matter Phys. 71 (2005) 036123. https://doi.org/10.1103/PhysRevE.71.036123.
- [10] F. Saulnier, T. Ondarçuhu, A. Aradian, E. Raphaël, Adhesion between a viscoelastic material and a solid surface, Macromolecules. 37 (2004) 1067–1075. https://doi.org/10.1021/ma021759t.
- [11] G.J. Lake, P.B. Lindley, Cut growth and fatigue of rubbers. II. Experiments on a noncrystallizing rubber, J. Appl. Polym. Sci. 8 (1964) 707–721. https://doi.org/10.1002/app.1964.070080212.
- [12] P.B. Lindley, Non-Relaxing Crack Growth and Fatigue in a Non-Crystallizing Rubber., Rubber Chem. Technol. 47 (1974) 1253–1264. https://doi.org/10.5254/1.3540497.

- [13] C. Creton, M. Ciccotti, Fracture and adhesion of soft materials: a review, Reports Prog. Phys. 79 (2016) 046601. https://doi.org/10.1088/0034-4885/79/4/046601.
- [14] R.S. Rivlin, A.G. Thomas, Rupture of rubber. I. Characteristic energy for tearing, J. Polym. Sci. 10 (1953) 291–318. https://doi.org/10.1002/pol.1953.120100303.
- [15] Y. Qi, J. Caillard, R. Long, Fracture toughness of soft materials with rate-independent hysteresis, J. Mech. Phys. Solids. 118 (2018) 341–364. https://doi.org/10.1016/J.JMPS.2018.05.020.
- [16] R. Long, C.-Y. Hui, Fracture toughness of hydrogels: measurement and interpretation, Soft Matter. 12 (2016) 8069–8086. https://doi.org/10.1039/C6SM01694D.
- [17] J.R. Rice, Mathematical Analysis in the Mechanics of Fracture, in: Liebowitz H. (Ed.), Fract. An Adv. Treatise, Vol.2, Mat, Academic Press, N.Y., 1968: pp. 191–311.
- [18] G.A.C. Graham, The correspondence principle of linear viscoelasticity theory for mixed boundary value problems involving time-dependent boundary regions, Q. Appl. Math. 26 (1968) 167–174. https://doi.org/10.1090/qam/99860.
- [19] R.A. Schapery, A theory of crack initiation and growth in viscoelastic media I. Theoretical development, Int. J. Fract. 11 (1975) 141–159. https://doi.org/10.1007/BF00034721.
- [20] W.G. Knauss, On the steady propagation of a crack in a viscoelastic sheet: experiments and analysis, in: H.H. Kausch, J.A. Hassell, R.I. Jaffee (Eds.), Deform. Fract. High Polym., Springer US, 1973: pp. 501–541. https://doi.org/10.1007/978-1-4757-1263-6 27.
- [21] C.Y. Hui, B. Zhu, R. Long, Steady state crack growth in viscoelastic solids: A comparative study, J. Mech. Phys. Solids. 159 (2022) 104748. https://doi.org/10.1016/J.JMPS.2021.104748.
- [22] J.R. Rice, The mechanics of quasi-static crack growth, in: R.E. Kelly (Ed.), Proceedins 8th U.S. Natl. Congr. Appl. Mech., Western Periodicals CO., 1978: pp. 191–126.
- [23] M. Ciavarella, G. Cricri, R. McMeeking, A comparison of crack propagation theories in

- viscoelastic materials, Theor. Appl. Fract. Mech. 116 (2021) 103113. https://doi.org/10.1016/J.TAFMEC.2021.103113.
- [24] B.N.J. Persson, On Opening Crack Propagation in Viscoelastic Solids, Tribol. Lett. 69 (2021) 1–8. https://doi.org/10.1007/S11249-021-01494-Y/FIGURES/6.
- [25] J.C. Simo, On a fully three-dimensional finite-strain viscoelastic damage model: Formulation and computational aspects, Comput. Methods Appl. Mech. Eng. 60 (1987) 153–173. https://doi.org/10.1016/0045-7825(87)90107-1.
- [26] R.A. Schapery, Correspondence principles and a generalized integral for large deformation and fracture analysis of viscoelastic media, Int. J. Fract. 1984 253. 25 (1984) 195–223. https://doi.org/10.1007/BF01140837.
- [27] R.A. Schapery, On the mechanics of crack closing and bonding in linear viscoelastic media, Int. J. Fract. 1989 391. 39 (1989) 163–189. https://doi.org/10.1007/BF00047448.
- [28] J.A. Greenwood, The theory of viscoelastic crack propagation and healing, J. Phys. D. Appl.
 Phys. 37 (2004) 2557–2569. https://doi.org/10.1088/0022-3727/37/18/011.

Supplementary Information

Dynamic effect in the fatigue fracture of viscoelastic solids

Qiang Guo¹, Julien Caillard², Davide Colombo², Rong Long^{1*}

Table of Contents

| S1. Energetic Fracture Criterion | 2 |
|--|----|
| S2. Finite Element Simulations of Crack Growth | 5 |
| S3. Actual and Phantom States: Stress Field | 11 |
| S4. Integral Equation for Crack Velocity | 15 |
| S5. Solution of the Crack Velocity | 19 |
| References | 22 |

¹Department of Mechanical Engineering, University of Colorado Boulder, CO 80309 USA.

²Manufacture Française des Pneumatiques Michelin, Centre de Technologies Europe, Clermont Ferrand Cedex 9, 63040, France

^{*}Corresponding author: rong.long@colorado.edu

S1. Energetic Fracture Criterion

To understand the role of viscoelastic dissipation in cyclic crack growth, we derive an isothermal and instantaneous energy balance equation for crack growth in a solid occupying a volume Λ and boundary surface Ω in the reference configuration. Following the procedures described in our recent work [1], we find that at any instant

$$\int_{\Omega} \mathbf{\Sigma} \cdot \frac{d\mathbf{u}}{dt} d\Omega - \int_{\Lambda} \left(\mathbf{P} : \frac{d\mathbf{F}}{dt} \right) d\Lambda = \Gamma_0 \frac{dA}{dt}, \tag{S1}$$

where Σ and \mathbf{u} are the traction and displacement vectors on the boundary Ω , \mathbf{P} is the first Piola-Kirchhoff stress tensor, \mathbf{F} is the deformation gradient tensor, Γ_0 is the Helmholtz free energy required to grow the crack by a unit area in the reference configuration, also known as the intrinsic fracture toughness (energy/area), and A is the area of crack surface. Equation (S1) states that the power of external tractions subtracted by the internal stress power is equal to the power consumed by crack growth. To make eq. (S1) valid for any finite deformation in general, we have adopted the first Piola-Kirchhoff stress \mathbf{P} and deformation gradient tensor \mathbf{F} . It is known from the continuum mechanics literature [2] that the incremental stress work \mathbf{P} :d \mathbf{F} is equal to \mathbf{S} :d \mathbf{E} , where \mathbf{S} is the second Piola-Kirchhoff stress tensor and $\mathbf{E} = (\mathbf{F}^T\mathbf{F} - \mathbf{I})/2$ is the Green-Lagrange strain tensor (\mathbf{I} is the identity tensor). Under infinitesmal deformation, \mathbf{S} :d \mathbf{E} (or equivalently \mathbf{P} :d \mathbf{F}) degenerates to $\mathbf{\sigma}$:d \mathbf{e} , where $\mathbf{\sigma}$ and \mathbf{e} are the linear stress and strain tensors, respectively. A version of eq. (S1) in terms of $\mathbf{\sigma}$ and \mathbf{e} can be found in Anderson [3].

For elastic solids, Eq. (S1) can be cast in terms of the J-integral [4]. First, we recognize that du vanishes on the displacement boundary Ω_d , which allows us to reduce the total boundary Ω in Eq. (S1) to only the traction boundary Ω_d . Second, for elastic solids we can define a strain energy density function such that $dW = \mathbf{P}:d\mathbf{F} = \mathbf{S}:d\mathbf{E}$. Combining these two points, we see that the left hand side of Eq. (S1) is essentially the rate of change of potential energy. For a two-dimenionsal crack, one can follow the derivation on Page 211-213 in Rice [4] or the Appendix A in Qi [1] to show that the rate of change of potential energy is equal to the J-integral multiplied by dA/dt.

To specialize eq. (S1) for the ideal "pure shear" geometry shown in Fig.1a of the main text, we make the following observations:

- The boundary surface Ω is either traction-free (i.e., $\Sigma = 0$) or subjected to a prescribed displacement **u** which solely depends on $\lambda (= \Delta/H)$.
- The crack area A is equal to the product of crack length c and specimen thickness b.
- After a transient stage, the cyclic crack growth reaches a *quasi-steady-state* where the stress and deformation tensors at a material point located at (x, y) only depend on its relative position to the crack tip and the time t. Because of the periodic nature of cyclic loading, the time t essentially reflects the external loading $\lambda (= \Delta/H)$, i.e., λ is a functions of t. Therefore, we can write $\mathbf{P} = \mathbf{P}^*(x-c(t), y, t)$ and $\mathbf{F} = \mathbf{F}^*(x-c(t), y, t)$, where c is the crack length defined as the horizontal coordinate of the crack tip in the fixed coordinate system x-y and varies with the time t.

Based on these observations, we rewrite eq. (S1) as

$$\left[\int_{\Omega} \mathbf{\Sigma} \cdot \frac{\mathrm{d}\mathbf{u}}{\mathrm{d}\lambda} \frac{\mathrm{d}\lambda}{\mathrm{d}t} \mathrm{d}\Omega - \int_{V} \left(\mathbf{P} : \frac{\partial \mathbf{F}}{\partial t}\right) \mathrm{d}V\right] - \left[\int_{V} \left(\mathbf{P} : \frac{\partial \mathbf{F}}{\partial c}\right) \mathrm{d}V + \Gamma_{0}b\right] \frac{\mathrm{d}c}{\mathrm{d}t} = 0. \tag{S2}$$

The first term of eq. (S2) represents the energy balance for cyclic loading in the absence of crack growth and should be equal to zero since we ignore inertial effects. This means that the second term in eq. (S2) must vanish as well. We introduce a moving coordinate system X-Y that is centered at the crack tip and translates with the crack, i.e., X = x - c and Y = y (see Fig. 1a of the main text). Using the *quasi-steady-state* condition, we write $\partial \mathbf{F}/\partial c = -\partial \mathbf{F}/\partial X$ and conclude that the following equation must be satisfied at any time during crack propagation:

$$\int_{-H/2}^{H/2} \int_{-\infty}^{+\infty} \left(\mathbf{P} : \frac{\partial \mathbf{F}}{\partial X} \right) dX dY = \Gamma_0.$$
 (S3)

Equation (S3) relies only on the *quasi-steady-state* condition for crack growth, and is valid for any material behavior regardless whether it is elastic or inelastic. Moreover, since the *steady-state* crack growth under static loading is a special case of the *quasi-steady-state* condition, eq. (S3) is valid for static loading as well.

Since this work focuses on linear viscoelasticity and infinitesmal deformation, we replace the incremental stress work P:dF by $\sigma:d\epsilon$, where σ and ϵ are the linear stress and strain tensors. Therefore, eq. (S3) becomes

$$\int_{-H/2}^{H/2} \int_{-\infty}^{+\infty} \left(\mathbf{\sigma} : \frac{\partial \mathbf{\epsilon}}{\partial X} \right) dX dY = \Gamma_0,$$
 (S4)

On this basis, we further propose the following energetic fracture criterion:

$$\begin{cases} V = 0 & \text{if } G_0 < \Gamma_0 \\ V \ge 0 & \text{if } G_0 = \Gamma_0 \end{cases} \text{ with } G_0 \equiv \int_{-H/2-\infty}^{H/2} \int_{-\infty}^{+\infty} \left(\mathbf{\sigma} : \frac{\partial \mathbf{\epsilon}}{\partial X} \right) dXdY$$
 (S5)

which is eq. (2) of the main text.

S2. Finite Element Simulations of Crack Growth

We built a *plane stress* model in ABAQUS according to the geometry shown in Fig. 2a of the main text. Unlike the ideal "pure shear" geometry with infinite width, in Finite Element (FE) simulations we have to implement finite dimensions. Specifically, the model dimensions are: width L = 90 mm and height H = 6 mm. Note that L >> H as required by the "pure shear" geometry. An initial crack with length c = 30 mm was introduced on the left side of the model. To simulate crack growth, a cohesive zone was introduced along the projected crack growth path directly ahead the original crack tip. The mesh near the crack propagation path was refined to improve accuracy with the smallest element size being 0.01 mm. To limit the number of elements and hence computational cost, only a region with length of 15 mm and height of 1.8 mm ahead of the initial crack tip was assigned the refined mesh. The mesh was formed by 2D quadrilateral, plane stress elements with reduced integration (CPS4R). A representative figure of the FE mesh is shown in Fig. S1a.

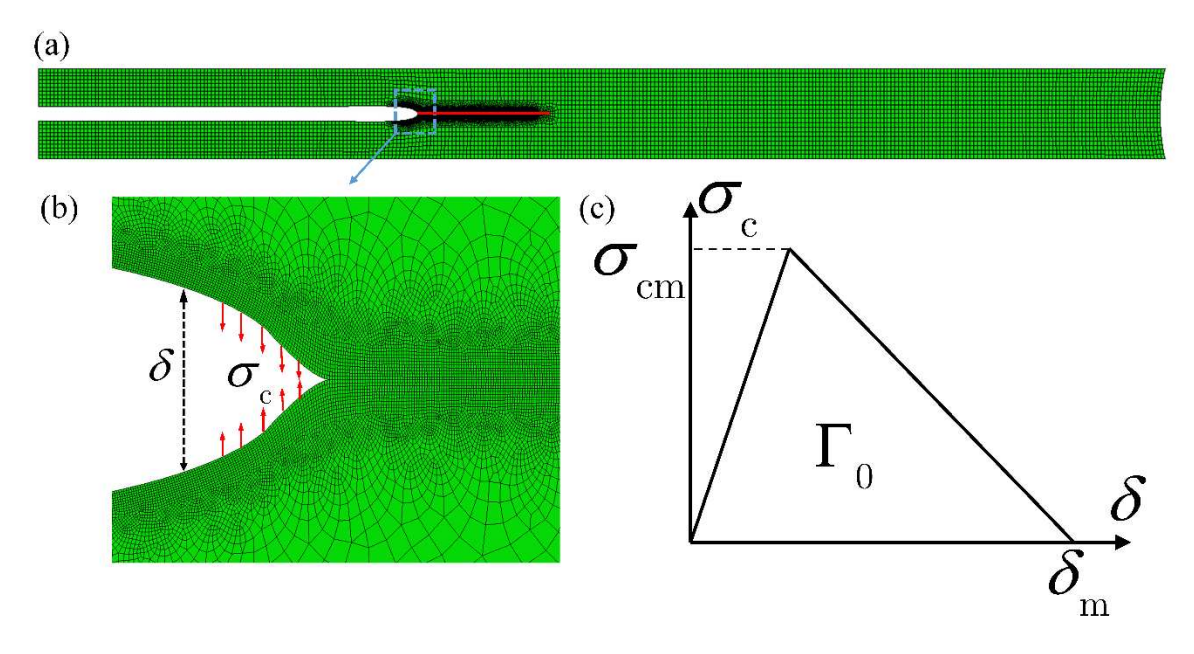


Figure S1 Geometry of FE model and cohesive zone. (a) Representative mesh of the FE model. (b) Zoomed-in view of the crack tip region under loading. The cohesive elements are not shown to improve readability. Instead, the cohesive traction σ_c is represented by red arrows and δ is the separate between the crack surfaces. (c) Bilinear traction-separation law for the cohesive zone featuring a peak cohesive traction σ_{cm} , maximum separation δ_m , and intrinsic fracture energy Γ_0 (i.e., area underneath the traction-separation curve).

The cohesive zone along the projected path of crack growth was implemented using a layer of cohesive elements. We adopted the bilinear traction-separation law as illustrated in Figs.S1b-S1c, which has been applied in the literature to study crack growth in inelastic soft materials [1,5]. This cohesive zone model featured a peak cohesive traction σ_{cm} , maximum separation δ_m , and intrinsic fracture energy Γ_0 . In our simulations we set $\sigma_{cm} = 2$ MPa, $\delta_m = 0.25$ mm and $\Gamma_0 = \sigma_{cm} \delta_m / 2 = 250$ J/m².

For the bulk material model, we implemented the viscoelastic model using Simo's approach of quasi-linear viscoelasticity [6]. This approach combines a hyperelastic model with a relative relaxation function g(t) (i.e., g = 1 at t = 0 and $g = g_{\infty}$ at $t = +\infty$). Although one can apply a Prony series for the relaxation function to capture the spectrum of relaxation times for practical viscoelastic solids, for simplicity we assumed a simple model as illustrated in Fig. 2b of the main text. In this case, the relative relaxation function is

$$g(t) = (1 - g_{\infty}) + g_{\infty} \exp\left(-\frac{t}{\tau}\right), \tag{S6}$$

where τ is the relaxation time and g_{∞} is the long-term relaxation ratio. The elastic springs in Fig.2b of the main text were modeled by the neo-Hookean solid with the following strain energy density function:

$$W = \frac{E}{6} \left(\overline{I}_1 - 3 \right) + \frac{\Psi}{2} \left(\det(\mathbf{F}) - 1 \right)^2, \tag{S7}$$

where E is the Young's modulus, Ψ is the bulk modulus, \mathbf{F} is the deformation gradient tensor, $\det(\mathbf{F})$ is the determinant of \mathbf{F} , and

$$\overline{I}_{1} = \left\lceil \det \left(\mathbf{F} \right) \right\rceil^{-2/3} tr \left(\mathbf{F} \mathbf{F}^{T} \right). \tag{S8}$$

Since most soft rubber and elastomers are approximately incompressible (i.e., Poisson's ratio close to 0.5), we assumed that the bulk modulus Ψ is much larger than E, specifically $\Psi = 4167E$. We assigned the neo-Hookean model to both springs in Fig.2b of the main text and set $E_1 = E_2 = 2.4$ MPa, which is equivalent to setting the instantaneous modulus as $E_0 \equiv E_1 + E_2 = 4.8$ MPa, the relaxed modulus as $E_\infty \equiv E_2 = 2.4$ MPa, and the relaxation ratio as $g_\infty = 0.5$. The relaxation time τ in eq. (S6) was left as a variable and we preformed simulations with different τ to study the effect

of ratio T/τ (recall that T is the loading cycle period). The viscoelastic model implemented in ABAQUS (Section 4.8.2 of ABAQUS Theory Guide) follows Simo's approach [6]. Here we briefly describe the formulation implemented in ABAQUS. The instantaneous Cauchy stress tensor, denoted as σ_0 , is first calculated based on the strain energy density function in eq. (S7), and is then decomposed into the hydrostatic part σ_0^S and deviatoric part σ_0^D , i.e.,

$$\mathbf{\sigma}_0 = \mathbf{\sigma}_0^S + \mathbf{\sigma}_0^D \text{ where } \mathbf{\sigma}_0^S = \frac{tr(\mathbf{\sigma}_0)}{3}\mathbf{I},$$
 (S9)

where I is the identity tensor. The deviatoric Cauchy stress over time is given by

$$\boldsymbol{\sigma}^{D}(t) = \boldsymbol{\sigma}_{0}^{D}(\mathbf{F}_{t}) + \operatorname{dev}\left[\mathbf{F}_{t}\left(\int_{0}^{t} \frac{dg(s)}{ds}(\mathbf{F}_{t-s})^{-1} \boldsymbol{\sigma}_{0}^{D}(\mathbf{F}_{t-s})(\mathbf{F}_{t-s})^{-T} ds\right)(\mathbf{F}_{t})^{T}\right], \quad (S10)$$

where \mathbf{F}_t is the deformation gradient tensor from time 0 to time t, \mathbf{F}_{t-s} is the deformation gradient tensor from time 0 to time t-s ($s \le t$), and g(t) is the relaxation function. The hydrostatic Cauchy stress over time $\sigma^S(t)$ is determined by enforcing the plane stress condition, i.e., the out-of-plane components of the total Cauchy stress $\sigma(t)$ must be zero.

The viscoelastic and cohesive parameters adopted in the FE model are justified as follows.

- Viscoelastic parameters: The long-term modulus E_{∞} was set to be 2.4 MPa as a typical value for elastomers. As discussed in the main text, E_0/E_{∞} was set to be relatively small (= 2) to limit the variation of cohesive zone size and hence facilitate the comparison between the FE model and theory. The relaxation time τ was varied to change the ratio of T/τ .
- Cohesive zone parameters: The maximum separation δ_m was set to be 0.25 mm, which is ~ 4% of the sample height (H=6 mm). This value was selected so that the cohesive zone is localized at the crack tip spanning over tens of elements. Recall that the element size near the crack tip was 0.01 mm. The localized cohesive zone is required so that the K-field based analysis of energy dissipation is valid. Further reduction of δ_m would require smaller element size at the crack tip and hence higher computational cost. The peak cohesive stress σ_{cm} was selected to be 2 MPa so that the intrinsic toughness Γ_0 (i.e., area underneath the cohesive traction-separation law), given by $\sigma_{cm}\delta_m/2=250$ J/m², is within the reasonable range of elastomers (on the order of 100 J/m²).

Using the FE model outlined above, we performed a series of FE simulations to study the rate of crack growth under static and cyclic loading. These simulations were carried out using the explicit dynamic solver (ABAQUS/Explicit) to accommodate the rapid unloading due to crack growth. We ensured that inertial effects in these simulations were negligible by using slow loading rates and mass scaling. Therefore, the simulations were still quasi-static, and the purpose of using the explicit dynamic solver was to circumvent the convergence problems with a static solver. When a vertical displacement Δ is applied to the sheet, the crack opens symmetrically and grows under sufficiently large Δ . Both static and cyclic loadings are considered in the simulations, as expressed in terms of the history of the nominal stretch ratio $\lambda \equiv 1 + \Delta/H$ (see Fig.2c of the main text).

We first considered static loading with prescribed nominal stretch $\lambda \equiv 1 + \Delta/H$ (ranging from 1.18 to 1.22). Figure S2 shows a representative set of simulation results for static loading. After an initial transient stage, the crack growth settled at a steady state with constant velocity V_s . As stated in the main text, we extracted the crack velocity V_s during the steady state and calculated the corresponding energy release rate using $G = \sigma_\infty \varepsilon_\infty H/2$. By varying the nominal stretch λ , we obtained a set of data points for G versus V_s (see inset of Fig.2d of the main text) and then applied polynomial fitting to generate an empirical function of $V_s(G)$. Note that we normalize V_s by δ_m/τ in the inset of Fig.2d, since τ is the only material time scale in the simulations and δ_m (i.e., maximum cohesive separation shown in Fig. S1c) is the relevant length scale for crack growth.

For cyclic loading, we imposed triangular periodic functions for $\lambda(t)$ that is bounded by λ_{min} = 1 and λ_{max} (ranging from 1.16 to 1.25) and has a period of T = 100s. Figure S3 shows a representative set of simulation results for cyclic loading. As shown in Fig.S3d, the cyclic crack growth rate dc/dN settled at a constant value. Note that the slight oscillation of dc/dN was due to the discretization of cohesive zone, since the crack only grew by a few elements per cycle. Following the idea of Lake and Lindley [7], we use the empirical function $V_s(G)$ obtained from static loading to predict the cyclic crack growth rate $(dc/dN)_s$ as follows

$$\left(\frac{\mathrm{d}c}{\mathrm{d}N}\right)_{s} = \int_{0}^{T} V_{s}\left(G(t)\right) dt, \qquad (S11)$$

where G(t) is obtained using the far-field stress and strain in the simulations with cyclic loading, i.e., $G(t) = \sigma_{\infty}(t)\varepsilon_{\infty}(t)H/2$. As stated in the main text, we quantify the dynamic viscoelastic effect by the ratio β :

$$\beta = \frac{\mathrm{d}c / \mathrm{d}N}{\left(\mathrm{d}c / \mathrm{d}N\right)_{s}}.$$
 (S12)

The results for β in Fig.2d in the main text confirm that viscoelasticity can result in the dynamic effect observed for cyclic crack growth.

Finally, although the FE model is based on a quasi-linear viscoelastic model that acounts for large deformation while our theory is based on linear viscoelasticity, discrepancy caused by this difference is insignificant due to the moderate peak stretch applied ($\lambda_{max} = \sim 1.2$) and the relatively weak material nonlinearity of the neo-Hookean model.

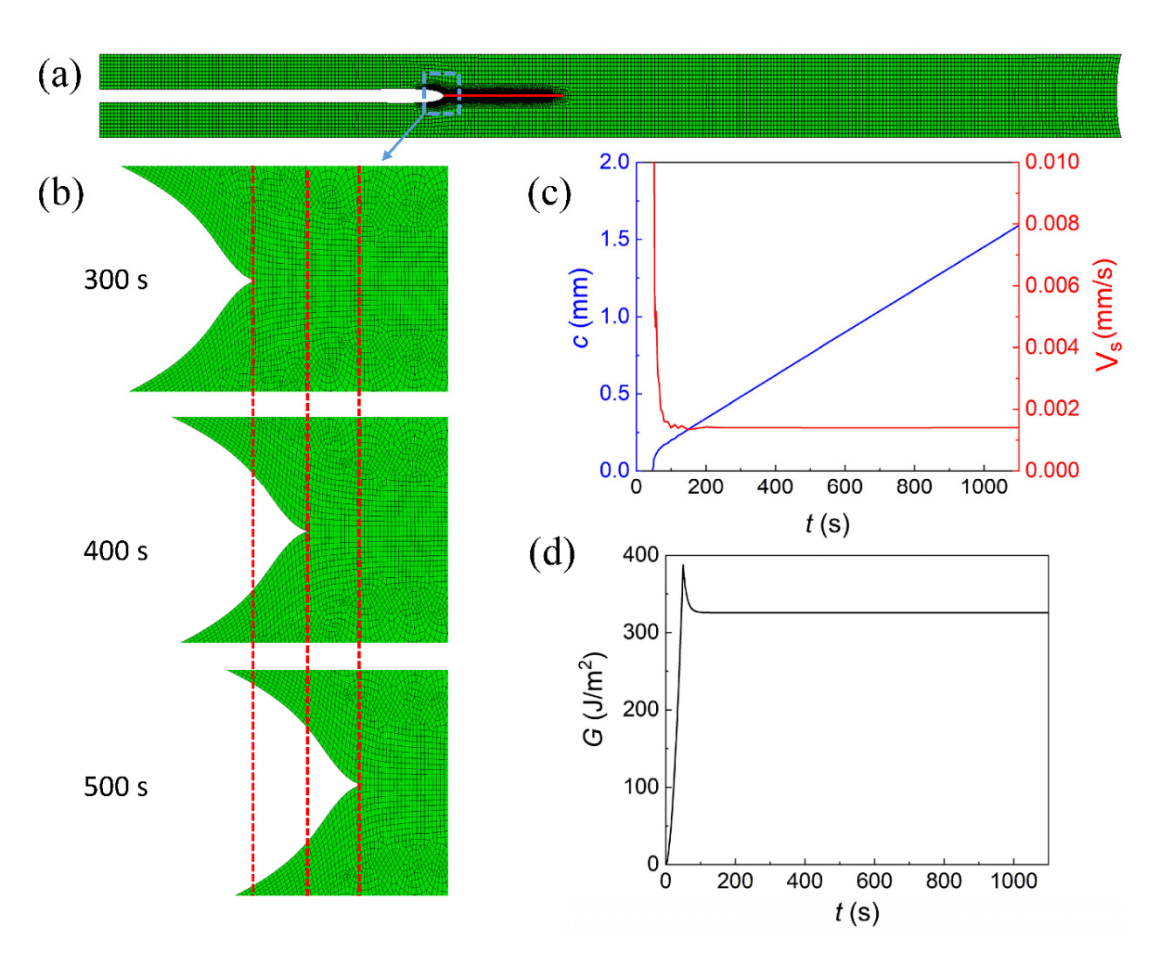


Figure S2 Representative FE results for static loading. (a) Deformed mesh during crack growth (b) Zoomed-in views of the crack tip region as the crack grows. (c) Crack length c and crack growth velocity V_s over time. A steady state emerges for t > 200s. For reference, the relaxation time is $\tau = 10$ s. (d) History of the energy release rate G. Crack growth occurs when $G \ge \Gamma_0 = 250$ J/m².

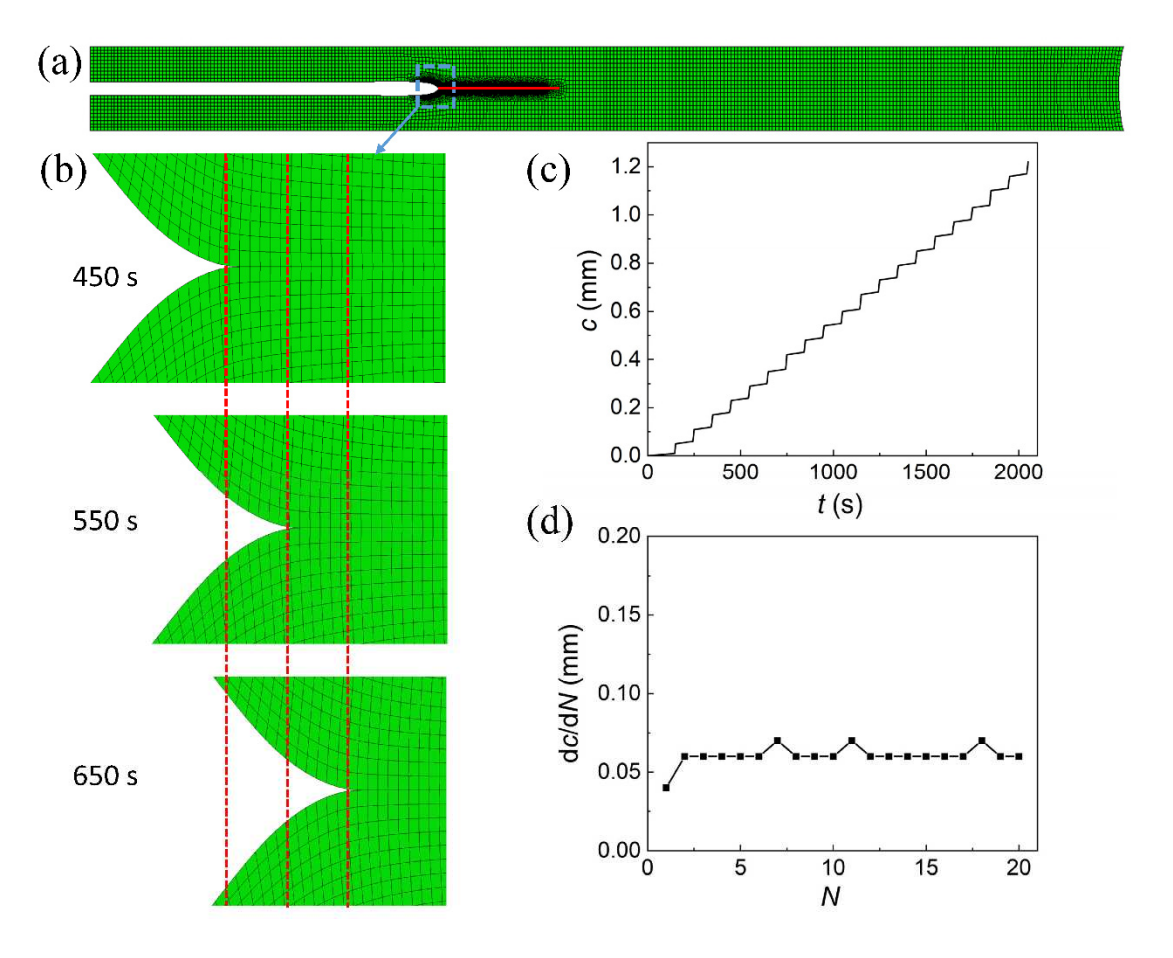


Figure S3 Representative FE results for cyclic loading. (a) Deformed mesh during crack growth (b) Zoomed-in views of the crack tip region as the crack grows. (c) Crack length c versus time t. For reference, the viscoelastic relaxation time is $\tau = 10$ s and the cycle period is T = 100 s. (d) Cyclic crack growth rate dc/dN over 20 loading cycles.

S3. Actual and Phantom States: Stress Field

We discuss the stress fields in the actual state (with crack growth) and the phantom state (without crack growth).

First, we use the extended correspondence principle by Graham [8] to conclude that the stress field near the crack tip in viscoelastic solids is the same as that in elastic solids. For scaling analysis, we neglect the effect of the fracture process zone (or equivalently, the cohesive zone) and adopt the *K*-field. The same approach has been adopted in the theories for steady-state crack growth under static loading by de Gennes [9], Saulnier et al. [10] and Persson & Brenner [11]. Specifically, for Mode-I crack, the *K*-field is given by

$$\begin{pmatrix} \sigma_{11} \\ \sigma_{22} \\ \sigma_{12} \end{pmatrix} = \frac{K}{\sqrt{2\pi R}} \cos \frac{\theta}{2} \begin{pmatrix} 1 - \sin \frac{\theta}{2} \sin \frac{3\theta}{2} \\ 1 + \sin \frac{\theta}{2} \sin \frac{3\theta}{2} \\ \sin \frac{\theta}{2} \cos \frac{3\theta}{2} \end{pmatrix}, \tag{S13}$$

where K is the stress intensity factor, R and θ are polar coordinates centered at the crack tip, and $R = \sqrt{X^2 + Y^2}$ and $\theta = \arctan(Y/X)$. Recall that we use $\sigma \equiv \sigma_{22}$ as the scaling representation of the entire stress field. At a given instant, the near-tip stress field can be written as

$$\sigma = \frac{K}{\sqrt{2\pi R}} \cos \frac{\theta}{2} \left(1 + \sin \frac{\theta}{2} \sin \frac{3\theta}{2} \right) = Kf(X, Y). \tag{S14}$$

Therefore, the near-tip stress field can be completely specified by the stress intensity factor K.

Second, by definition the stress field in the phamton state is identical to that in the actual state far away from the crack tip. This condition implies that the phantom and actual states should also share the same stress intensity factor K for the near-tip field. The agreement in both the far field and near-tip field suggests that the two states should share the same stress field at any given instant. As discussed in the main text, the difference between the two states is on the near-tip strain fields. Therefore, we focus on the near-tip fields given by eq. (S14) and write the phamton stress field $\bar{\sigma}$ and the actual stress field σ at an instant t as:

$$\bar{\sigma}(X,Y,t) = \sigma(X,Y,t) = K(t)f(X,Y). \tag{S15}$$

It should be emphasized that the cohesive zone may interact with the near-tip stress field, which can cause deviation from the *K*-field near the crack tip, as demonstrated in the cohesive zone approach by Knauss [12] or Schapery [13]. Such interaction may lead to difference in stress fields very close to the cohesive zone between the phantom and actual states. By adopting the *K*-field in eq. (S14), our scaling theory neglects this potential interaction.

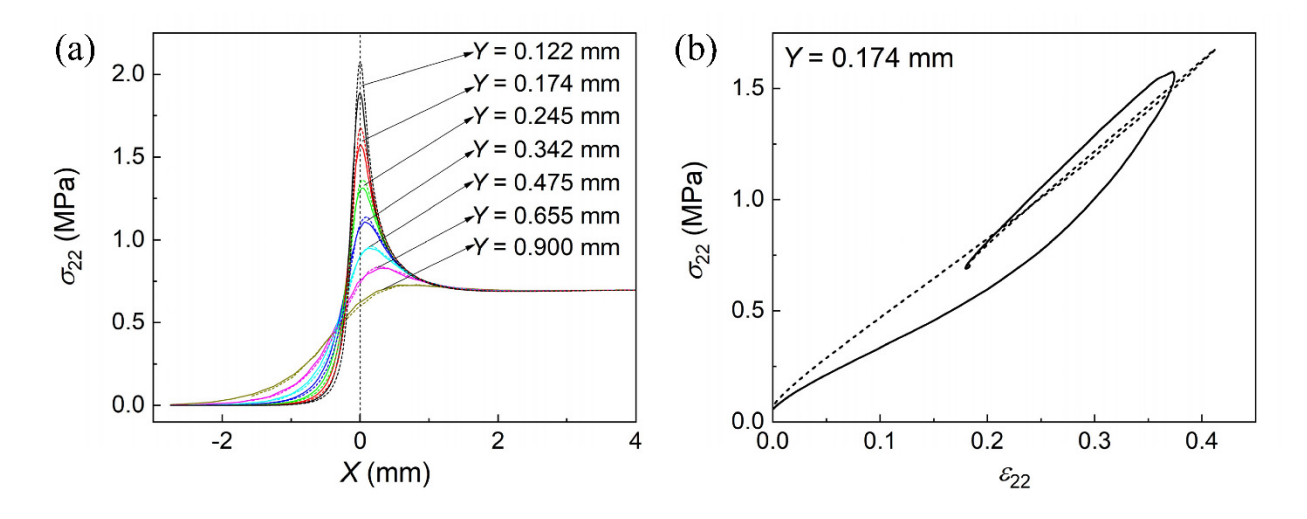


Figure S4 Stress distributions in the actual state and state. (a) Normal stress σ_{22} versus X along seven horizontal lines with different Y. (b) Normal stress σ_{22} versus normal strain ε_{22} along Y = 0.174 mm. The dashed lines represent results for the phantom state and the solid lines represent results for the actual state.

We verify the assumption of identical stress fields for the phantom and actual states using the FE results. The actual state (with crack growth) was obtained using the cohesive zone approach described in Section S2, while the phantom state (without crack growth) was obtained by substantially increasing σ_{cm} and Γ_0 of the cohesive zone model to suppress crack growth. In Fig.S4a, we plot the distributions of σ_{22} along seven horizontal lines (i.e., different Y) at the same time during a loading cycle. Recall that X = 0 is the vertical line passing through the crack tip. It can be seen that stress distributions for the two states are approximately the same. Deviations can be found near X = 0 with small Y. This is attributed to the different cohesive zone parameters employed for the two states. Specifically, the phantom state exhibits a larger stress near the crack tip due to the larger peak cohesive stress σ_{cm} used in the phantom state. Such deviations are expected since we have neglected the effects of cohesive zone by adopting the K-field. In Fig.S4b,

we plot the stress σ_{22} versus the strain ε_{22} along a horizontal line (Y = 0.174 mm), which is approximately the same as the schematic shown in Fig.1b of the main text. In particular, the spatial hysteresis in the phantom state is nearly zero, but is significant in the actual state. Again, the slightly discrepancy between Fig.S4b and Fig.1b of the main text is due to the different cohesive zone parameters employed to produce the actual and phantom states.

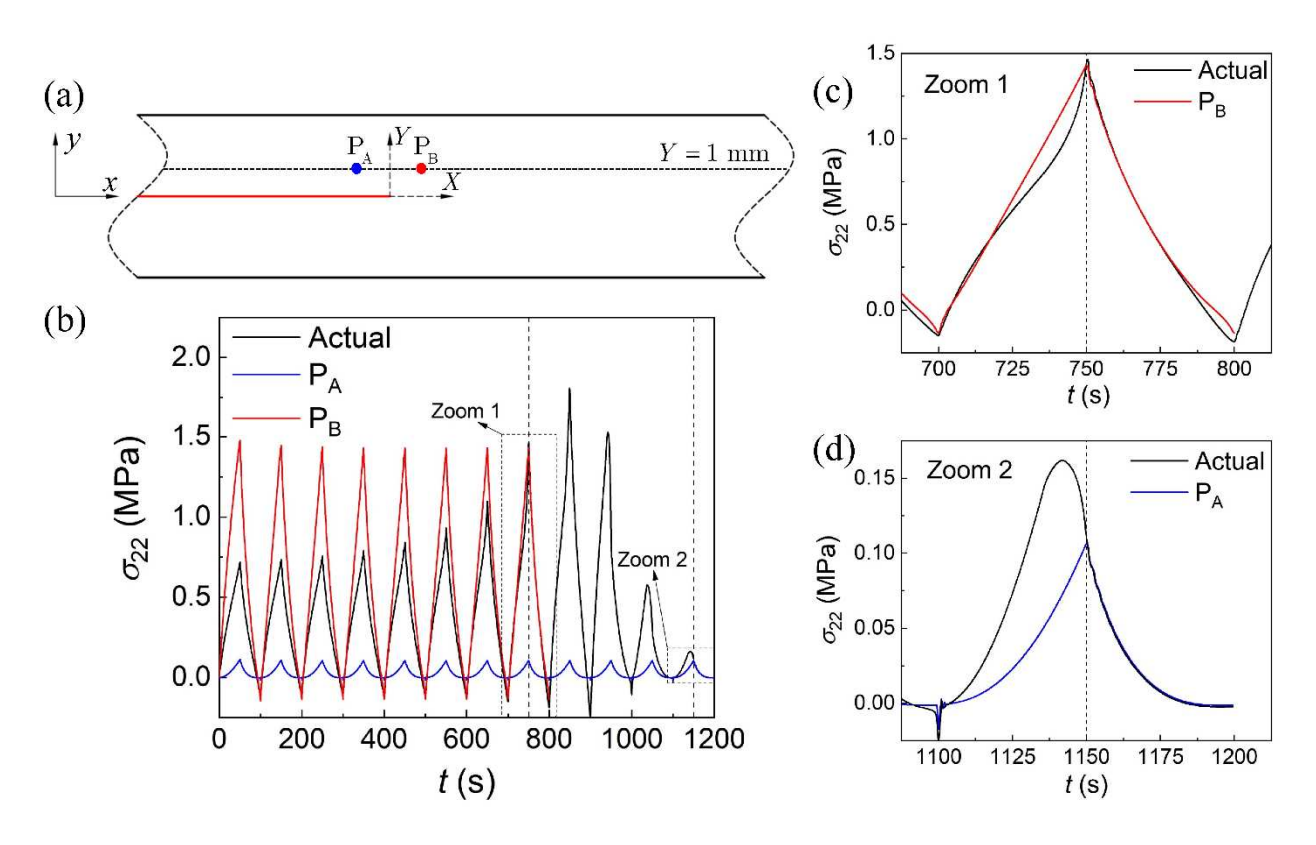


Figure S5 Stress history in the actual and phantom states. (a) Schematic of the "pure shear" geometry in the FE simulation. P_A and P_B are two points ahead of (X > 0) and behind (X < 0) the crack tip at Y = 1 mm. (b) We extract the stress history of a material point located at Y = 1 mm in the actual state (black line), and compare it to the stress histories at P_A (blue line) and P_B (red line) in the phantom state. (c-d) Zoomed-in view of the stress history to facilitate the comparison of stress history between the actual and phantom states.

Although the actual and phantom states share the same stress field at a given instant, they exhibit different strain fields near the crack tip. This is because material points in these two states experienced different stress histories. To illustrate this point, we use the FE simulations and compare the stress histories for the two states. As shown in Fig.S5b, the stress history experienced

by a material point (black line) follows a cyclic profile, but the amplitude first increases and then decreases as the crack tip approaches the material point and then passes it. Such advective effect due to crack growth is absent in the phantom state, as illustrated by stress histories at two points P_A (blue line) and P_B (red line) ahead of and behind the crack tip, respectively. Figure S5c shows that when the material point in the actual state is temporarily located at P_B (i.e., 750 s < t < 800 s), it has the same stress as that in the phantom state. However, the stress history experienced by the material point prior to t = 750 s is different from that in the phantom state. Similar observation is found in Fig.S5d.

To mathematically represent the advective effect in the actual state, we consider an abitrary material point located at (x, y) where x-y is a fixed coordinates system (see Fig.S5a). Without loss of generality, we set

$$x = X + c \text{ and } Y = y, \tag{S16}$$

where c is horizontal coordinate of the crack tip relative to the fixed x-y system, and can be regarded as the effective crack length. In the actual state, c is a function of time, i.e., c = c(t), and thus the stress history at t' prior to the current time t is

$$\sigma(x, y, t') = K(t') f(x - c(t'), y), \quad t' \le t.$$
 (S17)

In the phantom state that corresponds to the actual state at the current time t, c is the same as c(t) and remains unchanged for any prior time t. Therefore, we have

$$\overline{\sigma}(x, y, t') = K(t') f(x - c(t), y), \quad t' \le t.$$
 (S18)

Equations (S17) and (S18) can also be written in terms of the X and Y coordinates of the material point at the current t by using eq. (S16) with c = c(t):

$$\sigma(x, y, t') = K(t') f(X + c(t) - c(t'), Y) \text{ and } \overline{\sigma}(x, y, t') = K(t') f(X, Y), t' \le t, \quad (S19)$$

which is the form in the main text.

S4. Integral Equation for Crack Velocity

In linear viscoelasticity, the strain ε at a material point under unaxial tension can be expressed using the hereditary integral:

$$\varepsilon(t) = \int_{-\infty}^{t} J(t - t') \frac{d\sigma}{dt'} dt' = J_0 \sigma(t) + \int_{-\infty}^{t} \dot{J}(t - t') \sigma(t') dt', \qquad (S20)$$

where J(t) is the creep compliance function, $J_0 = J(t = 0)$ and $\dot{J} = dJ/dt$. Note that eq. (S20) implicitly assumes that $\sigma = 0$ at $t = -\infty$. This is not contradictory to the stress histories in eq. (S17) and (S18), because one can always set the time $t = -\infty$ to be before the start of cyclic loading. The principle of fading memory dictates that the transient stage can be neglected and we only need to consider the stress history in the quasi-steady state. Combining eq. (S20) with the stress histories in eq. (S17) and (S18), we obtain

$$\Delta\varepsilon(x,y,t) = \varepsilon(x,y,t) - \overline{\varepsilon}(x,y,t) = \int_{-\infty}^{t} \dot{J}(t-t')K(t') \Big[f(x-c(t'),y) - f(x-c(t),y) \Big] dt'. \quad (S21)$$

Note that $\sigma = \bar{\sigma}$ at the current time t.

To apply eq. (4) of the main text, we rewrite eq. (S21) in the local coordinates X and Y using x = X + c(t) and y = Y, i.e.,

$$\Delta\varepsilon(X,Y;t) = \int_{-\infty}^{t} \dot{J}(t-t')K(t') \Big[f(X+\Delta\varepsilon(t,t'),Y) - f(X,Y) \Big] dt', \qquad (S22)$$

where $\Delta c(t, t') \equiv c(t) - c(t')$. Substituting eq. (S22) into eq. (4) and using eq. (S14) gives

$$G - G_0 = -K\left(t\right) \int_{-H/2}^{H/2} \int_{-\infty}^{+\infty} \dot{J}\left(t - t'\right) K\left(t'\right) f\left(X, Y\right) \left[\frac{\partial f}{\partial X}\left(X + \Delta c\left(t, t'\right), Y\right) - \frac{\partial f}{\partial X}\left(X, Y\right)\right] dt' dX dY,$$
(S23)

which is eq. (5) in the main text. Equation (S23) is the general governing equation for quasi-steady-state crack growth (static or cyclic). Under cyclic loading, both G and K are periodic functions of time. If these two functions are given, one can numerically solve eq. (S23) to determine the crack length c(t) at the current time and hence obtain the cyclic crack growth rate dc/dN.

To obtain physical insights, we consider the limiting case of *slow crack growth*, i.e., V = dc/dt is small. Note that the creep compliance function J(t) can be written as $J(t) = J(t \rightarrow +\infty) + \tilde{J}(t)$ where $J(t \rightarrow +\infty)$ is the equilibrium portion and $\tilde{J}(t)$ is the non-equilibrium portion of the creep function. Therefore, we replace $\dot{J}(t)$ by $\dot{\tilde{J}}(t)$ to take advantage of the limit that $\tilde{J}(t \rightarrow +\infty) = 0$. $\dot{\tilde{J}}(t)$ is a decaying function with a characteristic time of τ_c . For example, for simple viscoelastic solid shown in Fig.2b (also known as the standard linear solid),

$$J(t) = \frac{1}{E_{\infty}} - \frac{E_0 - E_{\infty}}{E_{\infty} E_0} e^{-t/\tau_c}, \quad \tilde{J}(t) = -\frac{E_0 - E_{\infty}}{E_{\infty} E_0} e^{-t/\tau_c}, \quad (S24)$$

$$\dot{J}(t) = \dot{\tilde{J}}(t) = \frac{1}{\tau_c} \frac{E_0 - E_{\infty}}{E_{\infty} E_0} e^{-t/\tau_c},$$
 (S25)

where E_0 is the instantaneous modulus, E_{∞} is the relaxed modulus and τ_c is the characteristic creep retardation time. Note that τ_c is related to the relaxation time τ through $\tau_c = (E_0/E_{\infty})\tau$. Because of the decaying behavior of $\dot{f}(t)$, we only need to account for the integrand of eq. (S23) when t - t' is on the same order of τ_c . Consequently, $\Delta c(t, t')$ in eq. (S23) should scale as $V\tau_c$.

Under *slow crack growth*, $V\tau_c$ is a small value and hence $\Delta c(t, t')$ is small, which allows us to make the following approximation:

$$\frac{\partial f}{\partial X}(X + \Delta c(t, t'), Y) - \frac{\partial f}{\partial X}(X, Y) \approx \frac{\partial^2 f}{\partial X^2}(X, Y) \Delta c(t, t'). \tag{S26}$$

However, caution should be taken here because $\partial^2 f/\partial X^2$ is not bounded at the crack tip. Recall that the distribution function f(X,Y) has a square root singularity, i.e., $f \sim R^{-1/2}$ as $R \to 0$ (see eq. (S14)) where $R = \sqrt{X^2 + Y^2}$. The square root singularity renders the following scaling relation: $\partial^2 f/\partial X^2 \sim R^{-5/2}$. The approximation in eq. (S26) cannot be valid at the crack tip (R = 0) because of the singular higher order derivatives, e.g., $\partial^3 f/\partial X^3 \sim R^{-7/2}$. For this reason, we need to implement a cut-off length at the crack tip. This cut-off length, denoted as l, represents the size of the fracture process zone (or equivalently, the cohesive zone). For simplicity, we follow de Gennes [9] and assume l is a material constant. More detailed analyses have shown that l can be dependent on the crack velocity [10–12]. For eq. (S26) to be valid, we need to satisfy the following condition

$$\Delta c(t,t') \sim V \tau_c \ll \frac{\partial^2 f / \partial X^2}{\partial^3 f / \partial X^3} \sim l, \qquad (S27)$$

which formally specifies the *slow crack growth* limit as $V\tau_c \ll l$.

The approximation in eq. (S26) allows us to decouple the spatial and temporal integrals in eq. (S23), i.e.,

$$G - G_0 = -K(t) \int_{-\infty}^{t} \dot{\tilde{J}}(t - t') K(t') \Delta c(t, t') dt' \int_{-H/2 - \infty}^{H/2} \int_{-\infty}^{+\infty} f(X, Y) \frac{\partial^2 f}{\partial X^2}(X, Y) dX dY.$$
 (S28)

The spatial integral C_f can be readily evaluated. First, we expand the integration domain to infinity, since H >> l and f(X,Y) decays to zero as $R = \sqrt{X^2 + Y^2} \to \infty$. Second, we rewrite the integral in terms of the polar coordinates R and θ and use eq. (S14) to determine f. Third, we set the lower integration limit for R to be the cut-off length l. Consequently, we obtain

$$C_{f} = \int_{-H/2}^{H/2} \int_{-\infty}^{+\infty} f(X,Y) \frac{\partial^{2} f}{\partial X^{2}} (X,Y) dXdY = \int_{l}^{+\infty} \int_{-\pi}^{+\infty} f(R,\theta) \frac{\partial^{2} f}{\partial X^{2}} (R,\theta) Rd\theta dR = -\frac{27}{128} \frac{1}{l}.$$
 (S29)

Note that we only account for σ_{22} and ε_{22} in our scaling analysis. The numerical pre-factor in eq. (S29) would change if we include the multi-axial stress components in eq. (S13). Nevertheless, we can still write $C_f = -\alpha/l$ where α is a positive constant of order one.

Next, we use integration by parts in eq. (S28) and obtain

$$G - G_0 = -K(t)C_f \left[-\tilde{J}(t - t')K(t')\Delta c(t, t') \Big|_{-\infty}^{t} + \int_{-\infty}^{t} \tilde{J}(t - t') \left[\dot{K}(t')\Delta c(t, t') - K(t')\dot{c}(t') \right] dt' \right], \tag{S30}$$

where $\dot{K}(t) = dK/dt$ and $\dot{c}(t) = dc/dt$. The first term within the square bracket of eq. (S30) vanishes because $\tilde{J}(t \to +\infty) = 0$ and $\Delta c(t,t) = 0$. Therefore, we arrive at the following result

$$G - G_0 = -K(t)C_f \int_{-\infty}^{t} \tilde{J}(t - t') \left[\dot{K}(t')\Delta c(t, t') - K(t')V(t')\right] dt',$$
(S31)

where we have identified $\dot{c}(t')$ as the crack velocity V(t'). To further simplify eq. (S31), we assume *slow loading*, i.e.,

$$\frac{\dot{K}(t')}{K(t')} \ll \frac{V(t')}{\Delta c(t,t')} \qquad \text{for } t - t' \sim \tau_c.$$
 (S32)

Using eq. (S32), we reduce eq. (S31) to

$$G - G_0 = K(t)C_f \int_{-\infty}^{t} \tilde{J}(t - t')K(t')V(t')dt', \qquad (S33)$$

which is eq. (6) in the main text. Note that both C_f (see eq. (S29)) and $\tilde{f}(t)$ are negative, which ensures that the right-hand side of eq. (S33) is positive.

It should be emphasized that eq. (S33) is based on two assumptions: slow crack propagation and slow loading, as manifested in eq. (S27) and (S32). Using the scaling relation that $\Delta c(t, t') \sim V\tau_c$ for $t - t' \sim \tau_c$, we can rewrite eq. (S27) and (32) as

$$\frac{V}{l} << \frac{1}{\tau_c}$$
 for slow crack growth. (S34)

and

$$\frac{\dot{K}}{K} \ll \frac{1}{\tau_c}$$
 for slow loading. (S35)

These two conditions involve three time scales: external loading (K/K), viscoelastic relaxation $1/\tau_c$, and crack propagation V/l. It is interesting to note that Knauss [12] pointed out that the steady state solution under static loading is applicable to cases with non-static loading (e.g. cyclic loading) if the following condition is satisfied:

$$\frac{\dot{K}}{K} \ll \frac{V}{2l} \,. \tag{S36}$$

Neglecting the factor 1/2, this condition states that "differences between a steady state solution and a transient one arise only if significant speed changes occur during the time interval in which the crack passes through the cohesive zone" [12]. Comparison of eq. (S36) with our two

assumptions in eq. (S34) and (S35) implies that we can still capture the dynamic effects using eq. (S33) if $V/l \sim \dot{K}/K \ll 1/\tau_c$.

The *slow crack growth* and *slow loading* assumptions also imply that the far field is in the fully relaxed state. Recall that τ_c is the creep retardation time and is typically larger than the relaxation time τ . For the simple model in Fig.2b, τ_c is related to the relaxation time τ via $\tau_c = (E_0/E_\infty)\tau > \tau$. Therefore, $1/\tau_c < 1/\tau$, indicating that $\dot{K}/K \ll 1/\tau$. Since we apply a displacement boundary condition at the far field, the condition that $\dot{K}/K \ll 1/\tau$ implies that the viscoelastic solid in the far field should be in the fully relaxed state. Therefore, we can relate K(t) and G(t) using the relaxed modulus, i.e., $G(t) = (K(t))^2/E_\infty$ assuming plane stress conditions.

S5. Solution of the crack velocity

Before presenting the numerical solution of eq. (6), it is worth discussing the special case of static loading. In this case, both K and V are constants. Assuming the standard linear solid model in Fig.2b, we substitute eq. (S24) into eq. (S33) and obtain

$$G - G_0 = -K^2 V C_f \tau_c \frac{E_0 - E_{\infty}}{E_{\infty} E_0} \text{ for } \frac{V}{l} << \frac{1}{\tau_c}.$$
 (S37)

Using eq. (S29) to write $C_f \sim -1/l$ and introducing the ratio $\eta = E_0/E_\infty$, we have

$$G - G_0 = G_D \sim \frac{K^2}{E_0} \frac{V \tau_c}{l} (\eta - 1) \text{ for } \frac{V}{l} < \frac{1}{\tau_c}.$$
 (S38)

Equation (S38) recovers the scaling relation for slow crack growth in Saulnier et al. [10]. To cast eq. (S38) in the same form as that in Saulnier et al. [10], we replace τ_c by the relaxation time $(E_0/E_\infty)\tau = \eta\tau$ and use $G_0 = K^2/E_0$ which is obtained by assuming the crack tip is surrounded by unrelaxed solid with modulus E_0 . Therefore, eq. (S38) becomes

$$\frac{G_D}{G_0} \sim \frac{V\tau}{l} \eta (\eta - 1) \text{ for } V \ll \frac{l}{\eta \tau}.$$
 (S39)

If $\eta >> 1$, eq. (S39) becomes

$$\frac{G_D}{G_0} \sim \frac{\eta^2 V \tau}{l} \text{ for } V \ll \frac{l}{\eta \tau},$$
 (S40)

which is identical to equation (13) of Saulnier et al. [10]. Therefore, we have recovered the static solution in the slow velocity limit.

Under cyclic loading, we numerically solve eq. (6) in the main text (or eq. (S33)) by assuming a triangular periodic function for K(t) and determine G(t) using $G(t) = (K(t))^2/E_{\infty}$. This condition allows us to rewrite eq. (6) as:

$$\frac{K^{2}(t)}{E_{\infty}} - G_{0} = K(t) \left| C_{f} \right| \int_{-\infty}^{t} \tilde{J}(t - t') K(t') V(t') dt'. \tag{S41}$$

Next we introduce the normalization

$$\overline{t} \equiv \frac{t}{T}, \quad \overline{s} \equiv \frac{t'}{T}, \quad \overline{K} \equiv \frac{K}{K_{m}}, \quad \overline{V} \equiv V \left| C_{f} \right| \tau, \quad \overline{\tilde{J}} = E_{\infty} \tilde{J}$$
 (S42)

where T is the period of a loading cycle, K_m is the maximum value of K(t) in a loading cycle, and τ is the characteristic relaxation time. Therefore, eq. (S41) becomes

$$\overline{K}^{2}(\overline{t}) - \frac{G_{0}E_{\infty}}{K_{m}^{2}} = \frac{T}{\tau}\overline{K}(\overline{t})\int_{-\infty}^{\overline{t}} \overline{\tilde{J}}(T(\overline{t}-\overline{s}))\overline{K}(\overline{s})\overline{V}(\overline{s})d\overline{s}.$$
 (S43)

To formulate the numerical scheme, the loading history, provided in terms of $\overline{K}(\overline{t})$, needs to be divided into sufficiently small increments. To this end, the time \overline{t} is divided into small steps with a uniform step size $\Delta \overline{t}$. Without loss of generality, we assume the loading starts at $\overline{t} = 0$, i.e., K = 0 for $\overline{t} < 0$. At the k-th step with $\overline{t}_k = k\Delta \overline{t}$, we have

$$\overline{K}^{2}\left(\overline{t_{k}}\right) - \frac{G_{0}E_{\infty}}{K_{\text{us}}^{2}} = \frac{T}{\tau}\overline{K}\left(\overline{t_{k}}\right)\sum_{i=1}^{k} \left\{\overline{\tilde{J}}\left[\left(\overline{t_{k}} - \overline{t_{i}}\right)T\right]\overline{K}\left(\overline{t_{i}}\right)\overline{V}\left(\overline{t_{i}}\right)\Delta\overline{t}\right\}. \tag{S44}$$

with $\overline{t_i} = i\Delta \overline{t}$. Subsequently, it is straightforward to deduce the following iterative format for the normalized crack velocity $\overline{V}(\overline{t_k})$:

$$\overline{V}(t_{k}) = \frac{\overline{K}(\overline{t_{k}})}{T/\tau} - \frac{G_{0}E_{\infty}}{K_{m}^{2}} \frac{1}{(T/\tau)\overline{K}(\overline{t_{k}})} - \sum_{i=1}^{k-1} \left\{ \overline{\tilde{J}}\left[(\overline{t_{k}} - \overline{t_{i}})T \right] \overline{K}(\overline{t_{i}}) \overline{V}(\overline{t_{i}}) \Delta \overline{t} \right\}}{\overline{\tilde{J}}(0)\overline{K}(\overline{t_{k}}) \Delta t}.$$
(S45)

To implement numerical computation calculation, we need to apply the following conditions:

- Set the initial condition that $\overline{V} = 0$ at $\overline{t_1} = \Delta \overline{t}$.
- Substitute the creep function $\tilde{J}(t)$ using eq. (S24).
- Apply the fracture criterion in eq. (S5), i.e., we set $G_0 = \Gamma_0$ and calculate V for the current time step. If V turns out to be negative, it means that the K or G at the current time step is not sufficient to drive crack growth. Therefore, the negative value of V is reset to zero at the current time and we move on to the next time step.

The numerical solution depends on three dimensionless parameters: G_0E_∞/K_m^2 , E_0/E_∞ (also denoted as η) and T/τ . To facilitate comparison with the FE simulation results, we fix $G_0E_\infty/K_m^2=0.667$ and $E_0/E_\infty=2$, and vary T/τ from 2.5 to 100. Using eq. (S45), we numerically compute the crack velocity for 10 cycles, i.e., \overline{t} ranges from 0 to 10 with an increment size of $\Delta \overline{t}=0.05$. Because of the range of T/τ (≥ 2.5), we find that the numerical solution of \overline{V} rapidly settles to a periodic function with time after the first cycle, as shown in Fig.S6. Therefore, we take \overline{V} in the last cycle as the solution for the *quasi-steady-state* under cyclic loading.

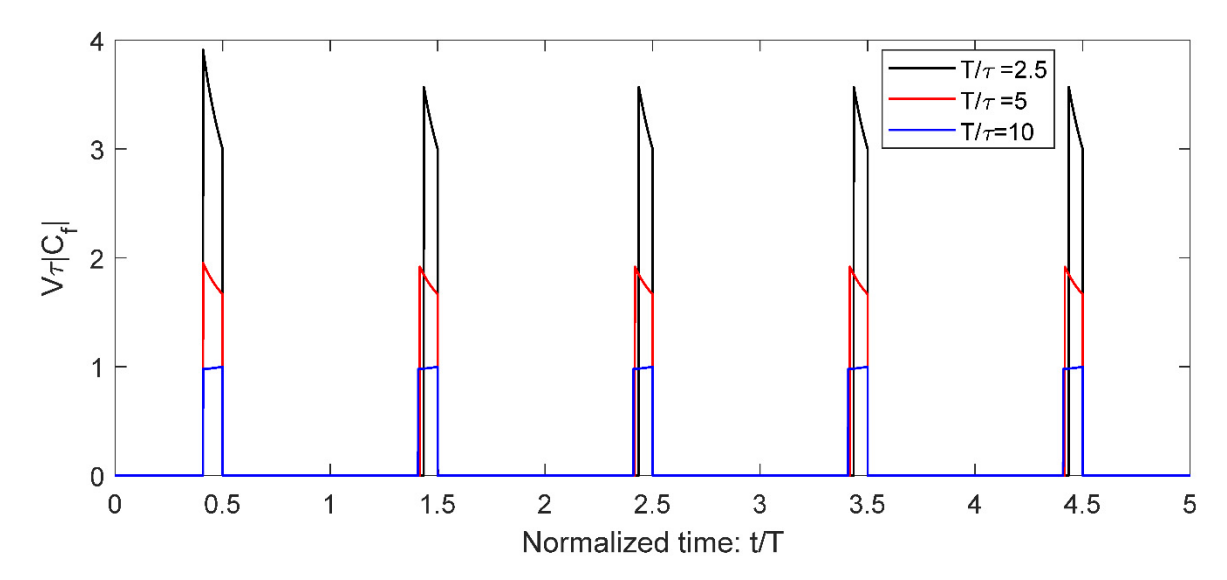


Figure S6 Numerical solution of crack velocity. Only the first five cycles out of the ten cycles are shown. The solutions are based on $G_0E_{\infty}/K_m^2=0.667$, $E_0/E_{\infty}=2$ and $T/\tau=2.5$, 5, or 10.

References

- [1] Y. Qi, J. Caillard, R. Long, Fracture toughness of soft materials with rate-independent hysteresis, J. Mech. Phys. Solids. 118 (2018) 341–364. https://doi.org/10.1016/J.JMPS.2018.05.020.
- [2] G.A. Holzapfel, Nonlinear solid mechanics: a continuum approach for engineering, Wiley, 2000.
- [3] T.L. Anderson, Fracture Mechanics: Fundamental and Applications, CRC Press, 2017.
- [4] J.R. Rice, Mathematical Analysis in the Mechanics of Fracture, in: Liebowitz H. (Ed.), Fract. An Adv. Treatise, Vol.2, Mat, Academic Press, N.Y., 1968: pp. 191–311.
- [5] T. Zhang, S. Lin, H. Yuk, X. Zhao, Predicting fracture energies and crack-tip fields of soft tough materials, Extrem. Mech. Lett. 4 (2015) 1–8. https://doi.org/10.1016/j.eml.2015.07.007.
- [6] J.C. Simo, On a fully three-dimensional finite-strain viscoelastic damage model: Formulation and computational aspects, Comput. Methods Appl. Mech. Eng. 60 (1987) 153–173. https://doi.org/10.1016/0045-7825(87)90107-1.
- [7] G.J. Lake, P.B. Lindley, Cut growth and fatigue of rubbers. II. Experiments on a noncrystallizing rubber, J. Appl. Polym. Sci. 8 (1964) 707–721. https://doi.org/10.1002/app.1964.070080212.
- [8] G.A.C. Graham, The correspondence principle of linear viscoelasticity theory for mixed boundary value problems involving time-dependent boundary regions, Q. Appl. Math. 26 (1968) 167–174. https://doi.org/10.1090/qam/99860.
- [9] P.G. de Gennes, Soft Adhesives †, Langmuir. 12 (1996) 4497–4500.https://doi.org/10.1021/la950886y.
- [10] F. Saulnier, T. Ondarçuhu, A. Aradian, E. Raphaël, Adhesion between a viscoelastic material and a solid surface, Macromolecules. 37 (2004) 1067–1075. https://doi.org/10.1021/ma021759t.
- [11] B.N.J. Persson, E.A. Brener, Crack propagation in viscoelastic solids, Phys. Rev. E Stat. Nonlinear, Soft Matter Phys. 71 (2005) 036123.

- https://doi.org/10.1103/PhysRevE.71.036123.
- [12] W.G. Knauss, A review of fracture in viscoelastic materials, Int. J. Fract. 196 (2015) 99–146. https://doi.org/10.1007/s10704-015-0058-6.
- [13] R.A. Schapery, A theory of crack initiation and growth in viscoelastic media II. Approximate methods of analysis, Int. J. Fract. 11 (1975) 369–388. https://doi.org/10.1007/BF00033526.